Article

Ultrasound-Activated Cascade Effect for Synergistic Orthotopic Pancreatic Cancer Therapy

Dong-Bing Cheng, Xue-Hao Zhang, Yuanfang Chen, Hao Chen, Zeng-Ying Qiao, Hao Wang

qiaozy@nanoctr.cn

HIGHLIGHTS

PPCs in single molecule state present remarkable solid-tumor penetrability

US induced *in situ* self-assembly of PPCs is verified

Assembled nanoparticles and US synergistically contribute to the cellular internalization

US-activated cascade effect leads to effective inhibition of pancreatic tumor growth

Article

Ultrasound-Activated Cascade Effect for Synergistic Orthotopic Pancreatic Cancer Therapy

Dong-Bing Cheng,[1] Xue-Hao Zhang,[1,2] Yuanfang Chen,[1] Hao Chen,[2] Zeng-Ying Qiao,[1,3,*] and Hao Wang[1]

SUMMARY

In some malignant tumor, especially for pancreatic tumor, poor solid-tumor penetration of nanotherapeutics impedes their treatment efficacy. Herein, we develop a polymer-peptide conjugate with the deep tissue penetration ability, which undergoes a cascade process under ultrasound (US), including (1) the singlet oxygen $^1O_2$ is generated by P18, (2) the thioketal bond is cleaved by the $^1O_2$, (3) the departure of PEG chains leads to the *in situ* self-assembly, and (4) the resultant self-assembled PK nanoparticles show considerable cellular internalization. Owing to the synergistic effect of US on increasing the membrane permeability, the endocytosis and lysosome escape of PK nanoparticles are further enhanced effectively, resulting in the improved therapeutic efficacy. Thanks to the high tissue-penetrating depth and spatial precision of US, PTPK presents enhanced tumor inhibition in an orthotopic pancreatic tumor model. Therefore, the US-activated cascade effect offers a novel perspective for precision medicine and disease theranostics.

INTRODUCTION

In cancer therapy, the pathological barrier and heterogeneity of tumor impair the delivery of chemotherapeutics into the tumor cells (Hida et al., 2016; Junttila and de Sauvage, 2013; Rosenblum et al., 2018). Most of the tumors, especially pancreatic tumor, are filled with and surrounded by the dense stroma, which contributes to interstitial pressures and decreases the blood perfusion, which hampers drugs attacking the tumor cells (Elgogary et al., 2016; Halbrook and Lyssiotis, 2017; Zhu et al., 2017). Although modifications of the cellular and acellular microenvironment have been achieved to ameliorate vascularization and tumor responses, it is still farfetched for chemotherapy owing to the low tumor accumulation of drugs. Besides, in some cases, tumor cells may become more aggressive after sweeping away the stroma or promoting vascularization (Tao et al., 2018; Han et al., 2018). Therefore, it is urgent to develop an effective platform for achieving both high accumulation and penetration in tumors.

Compared with the conventional chemotherapy, nanodrugs with prolonged circulation time and targeting effect have been approved to overcome both systemic and tumor tissue barriers potentially (Sun et al., 2017; Blanco et al., 2015; Cheng et al., 2017; Vankayala and Hwang, 2018; Guan et al., 2016; Zhang et al., 2014, 2018). Although the nanoparticle can deliver the drug to tumor tissue, there are still many critical deficiencies in treatment of pancreatic cancer, such as poor solid-tumor penetration and undesired uptake by normal cells. According to previous reports, in poorly permeable hypovascular tumors, nanodrugs with small particle size present efficient extravasation and penetrability (Peng et al., 2019; Dehaini et al., 2016; Ji et al., 2018; Wang et al., 2016). However, the dynamic extravasation in tumor may result in inefficient tumor accumulation or internalization (Matsumoto et al., 2016; Liu et al., 2013). Recently, the "*in vivo* self-assembly" strategy has been approved to realize both high accumulation and deep penetration in tumors (Cong et al., 2019; Zhang et al., 2015).

Considering the insufficient endogenous stimulation, exogenous stimuli are regarded as promising alternative cancer-therapy protocols, since they can be performed on the designated tumor spot, protecting the normal tissue/cells from damage (Blum et al., 2015; Li et al., 2016; Meng et al., 2016; Yang et al., 2019). The non-invasive photo-responsive drug delivery system has been approved to suppress tumor growth effectively, and some photosensitizers are already applied in clinical trials (Liu et al., 2017; Yuan et al., 2016; Celli et al., 2010; Zheng et al., 2016). However, the limited penetration depth of near-infrared
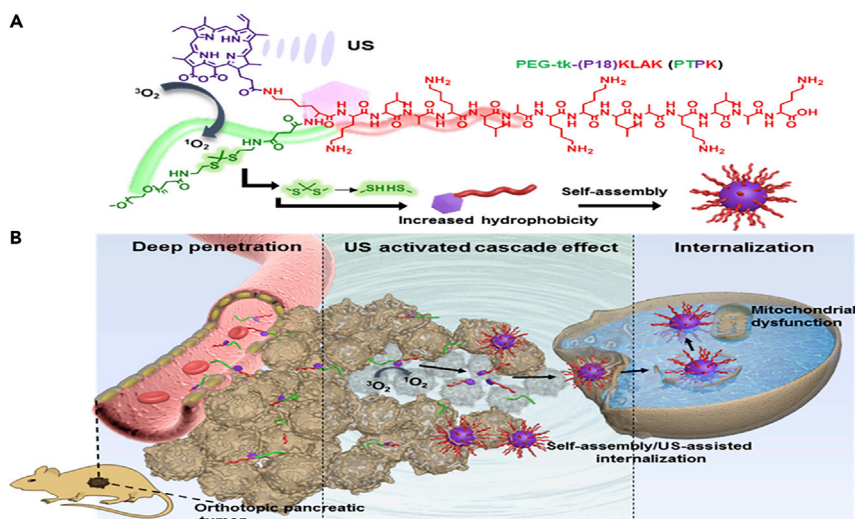
Scheme 1. Schematic Illustration of Ultrasound (US)-Activated Cascade Effect of Polymer-Peptide Conjugates for Orthotopic Pancreatic Cancer Therapy

(A) Molecular structure of PTPK and its US-activated cascade effect.

(B) Deep penetration of PTPK and US-induced cascade effect for synergistic cellular internalization and efficient tumor growth inhibition.

(NIR) light radiation severely restricts the further clinical application, since only the superficial and endoscopically reachable tumors can be inhibited. As a mechanical wave, ultrasound (US) is widely applied in diagnosis, imaging, and disease treatment (Song et al., 2016; Min et al., 2016; Gao et al., 2017). Compared with NIR light, US possesses high tissue-penetrating depth and spatial precision owing to the nonradiative property and low tissue attenuation coefficient, which can realize the treatment of deep-set disease, such as pancreatic cancer. Therefore, sonodynamic therapy (SDT), as a novel anticancer strategy, has been investigated recently (McEwan et al., 2015; Nomikou et al., 2017; Deepagan et al., 2016). Unfortunately, the sonosensitizers with insufficient SDT efficiency usually require the treatment to be at high dosage, causing the potential phototoxicity and skin sensitivity (Qian et al., 2016; Wu et al., 2019; Lin et al., 2020). Inspired by the advantage of US and disadvantage of SDT, we hypothesize a new *in vivo* self-assembly strategy, wherein US is used for triggering a cascade process, causing synergistic anticancer effect in orthotopic pancreatic tumor models.

Herein, we demonstrate the US-activated cascade process of polymer-peptide conjugates (PPCs) for deep penetration and effective endocytosis in pancreatic tumor, thus suppressing tumor growth efficiently. As shown in Scheme 1, sonosensitizer (purpurin 18, P18) decorated cytotoxic peptide (KLAK, sequence: $_D$-(KLAKLAK)2) is tethered with hydrophilic poly (ethylene glycol) (mPEG) via singlet oxygen $^1O_2$-cleavable thioketal bond to obtain the resultant conjugates PEG-tk-(P18)KLAK (PTPK). The hydrophilic PTPK can dissolve as a single chain in blood circulation, displaying efficient tumor penetrability. After precise US focusing on the tumor site, the $^1O_2$ produced by sonosensitizer P18 triggers the thioketal bond cleavage (Yuan et al., 2014; Zhang et al., 2019), and the enhanced hydrophobicity results in the self-assembly. The assembled PK nanoparticles and improved permeability of cell membrane synergistically contribute to the high internalization efficiency, thus inducing the cancer cell apoptosis by mitochondrial disruption. As a result, the subcutaneous and orthotopic pancreatic tumor models are established to demonstrate the significant advantages of US-induced cascade effect *in vivo*.

RESULTS

Molecular Design and Self-Assembly Behavior

The US-cleavable molecule PTPK and US-inert molecules PEG-(P18)KLAK (PPK) and (P18)KLAK (PK) are prepared according to the standard solid-phase peptide synthesis techniques (Scheme S1), wherein the mPEG-tk-COOH is obtained from our previous reports (Cheng et al., 2019). The structures of conjugates are confirmed by matrix-associated laser desorption ionization time-of-flight mass spectrometry (MALDI-TOF-MS) and ^1H NMR spectra (Figures S1–S3).
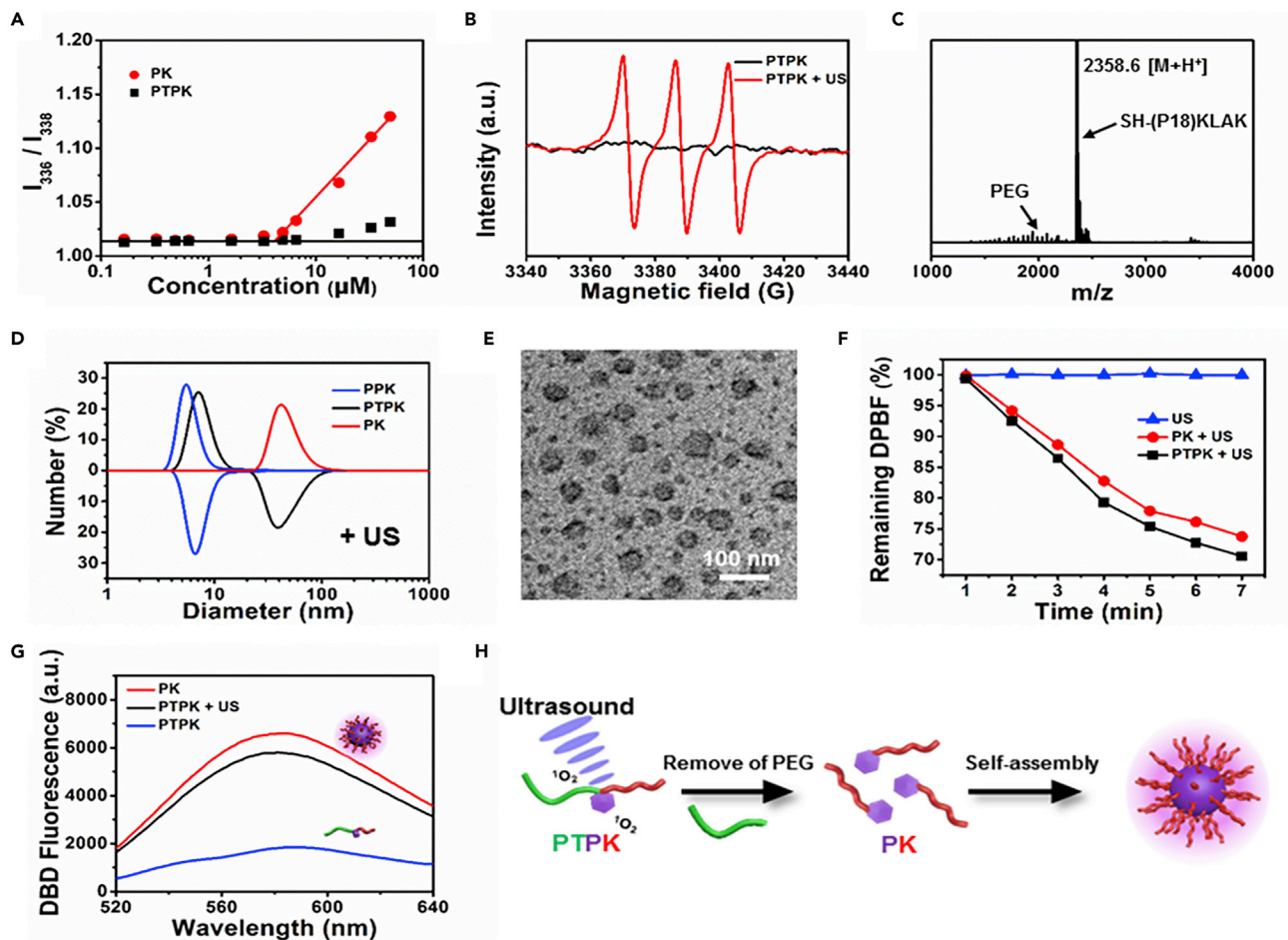
Figure 1. Self-Assembly Behavior of PTPK under US Irradiation

(A) CAC values determined by I_{336}/I_{338} ratio from pyrene as a function of concentration of PTPK.

(B) ESR spectra of PTPK (10 μM) with or without US irradiation.

(C) MALDI-TOF-MS of $^1O_2$-responsive PTPK after exposed to US irradiation. Calculated molecular weight of peptide residue SH-(P18)KLAK after cleavage is 2,357.9.

(D) Particle size of PTPK, PPK, and PK (10 μM) with or without US treatment in PB (0.01 M, pH 7.4) measured by DLS.

(E) Representative TEM images of PTPK under US irradiation for 10 min at 4 h.

(F) Changes of DPBF absorbance under US irradiation over various time durations.

(G) The fluorescence spectra of DBD-labeled PTPK and PK (10 μM) under US irradiation for 10 min.

(H) Schematic illustration of US-induced cascade effect.

The assembly ability of PPCs is first investigated by critical aggregation concentration (CAC). It is found out that the CAC of PTPK is higher than 50 μM in phosphate buffer (PB) solution, whereas PK possesses the CAC of 4.2 μM (Figure 1A), which suggests the molecular transition from PTPK (10 μM) to PK can realize *in situ* self-assembly in aqueous solution. The thioketal bond in PTPK is sensitive to $^1O_2$, and the electron spin resonance (ESR) spectroscopy is acquired to measure the $^1O_2$ generation (Figure 1B). 2,2,6,6-Tetramethyl-piperidine (TEMP) is employed as the spin-trapping reagent, and the characteristic 1:1:1 triplet signal is observed after the PTPK is exposed to US irradiation, which demonstrates the generation of $^1O_2$ (Huang et al., 2017). Subsequently, the $^1O_2$ responsiveness of PTPK is validated by MALDI-TOF-MS (Figure 1C), and the residue SH-(P18)KLAK is generated upon exposure to US. The self-assembly behavior of PTPK under US irradiation is clarified by dynamic light scattering (DLS) (Figure 1D). The particle sizes of PTPK increase from 7 ± 2 to 38 ± 4 nm, and the final size is close to the size of PK (41.2 nm) in PB solution. On the contrary, the particle size of non-responsive PPK shows no obvious change under the US. Transmission electron microscopy (TEM) observation further reveals that, after expose to US for 10 min, PTPK can self-assemble into well-dispersed nanoparticles, and the corresponding particle size (37 ± 5 nm) is similar to

DLS result (Figure 1E). All the results imply that the US can activate the self-assembly process, and the mechanism is further studied by fluorescence and UV-vis spectra. 1,3-Diphenylisobenzofuran (DPBF) assay is performed to quantitatively analyze the $^1O_2$ generation of PTPK and PK. DPBF can be oxidized by $^1O_2$, and its UV-vis absorbance intensity is attenuated (Figure 1F) (He et al., 2019). The absorbance intensity at 410 nm of DPBF decreases significantly when PTPK and PK are exposed to US for 7 min, which demonstrates the $^1O_2$ production of P18 during the US treatment. To study the drive force of self-assembly, polarity-sensitive fluorescence probe carboxylated 4-(2-aminoethylamino)-7-(N, N- dimethylsulfamoyl) benzofurazan (DBD-COOH) is labeled on PTPK. As shown in Figures 1G and S4, DBD-labeled PTPK exhibits a significant fluorescence increase after being exposed to US irradiation and the green dotted DBD fluorescence can be observed by confocal laser scanning microscopy (CLSM), which suggests the enhanced hydrophobicity of residue PK. The state of hydrophobic P18 moiety in the core of PK nanoparticles is investigated by CD and UV-vis spectra. Other than P18 aggregation, the disappearance of bisignate signals and sharp Qy band around 700 nm (Figure S5) are observed, demonstrating negligible π-π stacking in single-stranded PTPK and aggregated PK (Li et al., 2016a). Therefore, US can activate the cascade effect, including (1) the production of $^1O_2$, (2) the cleavage of PEG chains, and (3) the self-assembly triggered by hydrophobicity increase (Figure 1H).

In Vitro Cytotoxicity Mechanism and Tissue Penetration Evaluation

The cellular internalization of PPCs exposed to US is monitored by CLSM (Figures 2A, S6, and S7). It is clearly shown that red fluorescence cannot be observed when Panc-1 cells are incubated with Cy5-labeled PTPK for 4 h. After being exposed to US irradiation, the PTPK-treated cells show obvious red signal. Meanwhile, DBD-labeled PTPK is incubated with the Panc-1 cells for 4 h, and we observed high green fluorescence signal from DBD in cells (Figure S8). The results indicate PTPK can form nanoparticles upon exposure to US, which possess a higher internalization capacity by cellular endocytosis pathway. Moreover, compared with the Cy5-labeled PK group, the red signal intensity in cells incubated with Cy5-labeled PTPK under US irradiation is stronger (about 2-fold, Figure S6B), and more red fluorescence separates from the green fluorescence (LysoTracker) (lower overlap coefficient, Figure S6C), indicating that PTPK can easily enter cells and escape from the lysosomes into the cytoplasm during US treatment. US can enhance the cellular internalization of nanoparticles, which is known as "sonochemical internalization," since the reactive oxygen species (ROS)-induced lipid peroxidation increases the membrane permeability (Gonzales et al., 2016). Furthermore, the self-assembled nanoparticles can be observed in the lysosomes by Bio-TEM, confirming the *in situ* self-assembly under US (Figure 2B). Therefore, the cellular internalization is enhanced by self-assembly of PTPK and US-induced membrane permeability increases synergistically.

We speculate that both the efficient cellular internalization and the *in situ* self-assembly contribute to therapeutic activity of cytotoxic peptide, and hence the cytotoxicity against Panc-1 was investigated by CCK-8 assay (Figure 2C). Contrary to non-sensitive PPK, PTPK displays considerable cytotoxic activity under US irradiation, proving the effectiveness of self-assembly. More importantly, the PTPK + US group exhibits higher cytotoxicity than the PK nanoparticles group, which reveals that self-assembly and US can enhance internalization synergistically, resulting in the improved anticancer ability. In addition, the JC-1 assay was conducted to verify the mitochondria-regulated cell apoptosis (Figure S9). After incubation with PTPK for 12 h, Panc-1 cells under US irradiation shows obvious green fluorescence and low red fluorescence, similarly to the positive control carbonyl cyanide 3-chlorophenylhydrazon (CCCP) group. Compared with the PK group, the PTPK + US group suggests higher mitochondrial disruption ability. In contrast, the PPK, PPK + US, and PTPK groups show negligible mitochondrial disruption. All the results are in accordance with cytotoxicity, confirming that the synergistic internalization of PPCs under US causes the enhanced mitochondria-regulated cytotoxicity.

In order to explore the penetration ability of PTPK into tissue, multicellular tumor spheroid (MCS) of Panc-1 cancer cells are developed to simulate the solid tumor. As shown in Figures 2D and S10, after MCS is incubated with Cy5-labeled PK and PTPK for 8 h, red fluorescence signals are detected at different depths. Fluorescence signal of Cy5-labeled PK significantly reduces at the depth of 120 μm and almost disappears in the interior at 150 μm. By contrast, red fluorescence from Cy5-labeled PTPK reaches the interior of the MCS (~150 μm) with homogeneous intensity, suggesting the deep tissue permeability of single-stranded PTPK (Figure 2E). Moreover, the double (Cy5 and DBD)-labeled PTPK and PPK are applied to verify the self-assembly upon US irradiation in MCS (Figure 2F). Although the homogeneous red fluorescence disperses all over the MCS treated by PPK, almost invisible green fluorescence can be observed. Different from the
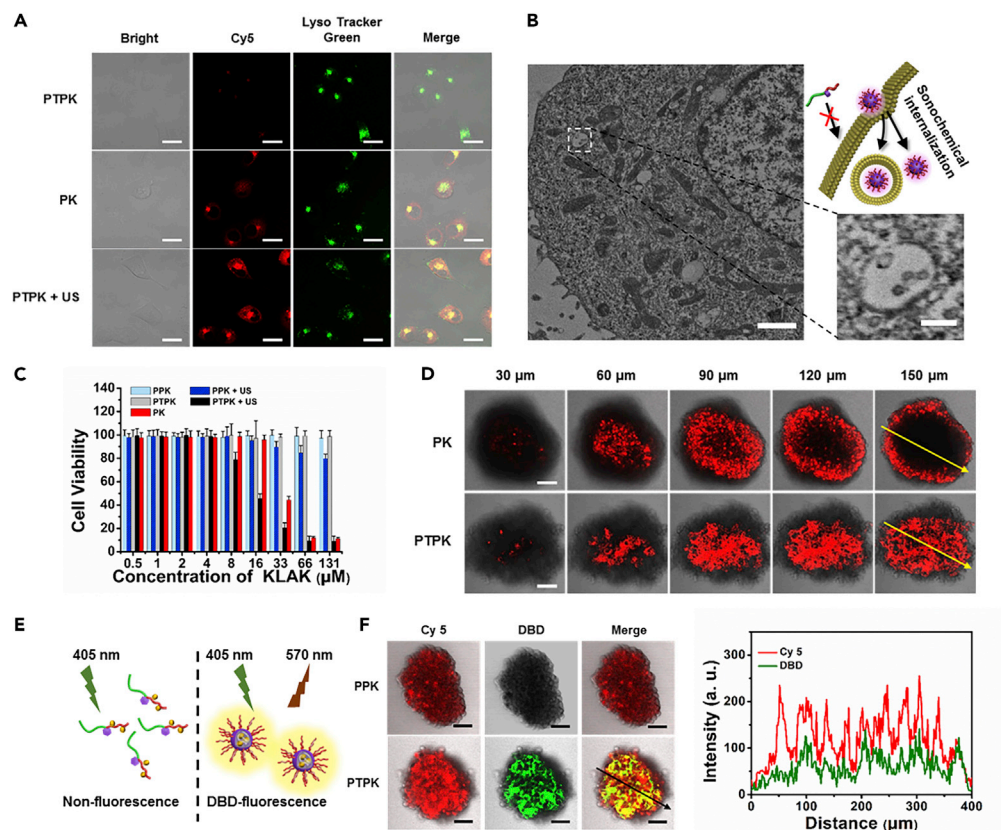
Figure 2. Cellular Internalization, Deep Penetration, and *In Situ* Self-Assembly of PPCs

(A) CLSM images of Panc-1 cells treated with Cy5-labeled PTPK and PK (10 μM for KLAK) with or without US treatment within 4 h Cy5 (red): 633 nm; LysoTracker (green): 488 nm. Scale bar: 20 μm.

(B) Bio-TEM images of Panc-1 cells incubated with PTPK after US irradiation (1.0 MHz, 1.5 W/cm^2, 50% duty cycle, 1 min) for 8 h. Scale bar: 1 μm (left); 400 nm (right).

(C) Cell viability of Panc-1 cells incubated with PTPK, PPK, or PK with or without US treatment measured by CCK-8 assay. The results are shown as means ± SEM. (N = 3).

(D) CLSM images of MCS treated by Cy5-labeled PTPK or PK for 8 h (10 μM for KLAK). Scale bar: 100 μm. Quantitative fluorescence analysis of the drawing line is shown in Figure S9.

(E) Schematic diagram of the self-assembly of DBD-labeled PPCs.

(F) CLSM images (left) and corresponding quantitative fluorescence analysis (right) in the drawing line of MCS treated by double-labeled PPCs under US irradiation. Scale bar: 100 μm

PPK group, MCS treated by PTPK shows obvious green DBD fluorescence, and quantitative fluorescence analysis further demonstrates the DBD fluorescence overlap well with Cy5 fluorescence. It is deduced that the favorable permeability of PTPK is attributed to the single chain state, and then upon the exposure to US, the divorced PEG causes the self-assembly due to the enhanced hydrophobicity. In addition, the red fluorescence intensity of MCS treated by PTPK under US is stronger than that treated by PPK. We speculate that the *in situ* self-assembly of PTPK and US can improve the endocytosis synergistically, resulting in the enhanced accumulation in MCS. Combining the deep penetration of single chain and high cellular uptake of nanoparticles, the PPCs with US-induced cascade effect may overcome pathological barrier and obtain efficient therapeutic efficacy against hypovascular solid tumor *in vivo*.

Tumor Accumulation and Penetration under US Irradiation

The tumor accumulation and penetration of PTPK under US irradiation are evaluated in Panc-1 subcutaneous xenograft mouse model, which is a representative intractable solid tumor, characterized by low vascularization and reduced vascular permeability due to pericyte coverage of blood vessels and thick fibrosis. Cy-5 labeled PPK, PK, PTPK, or PBS are intravenously (i.v.) injected into Panc-1 tumor-bearing mice, and the fluorescence
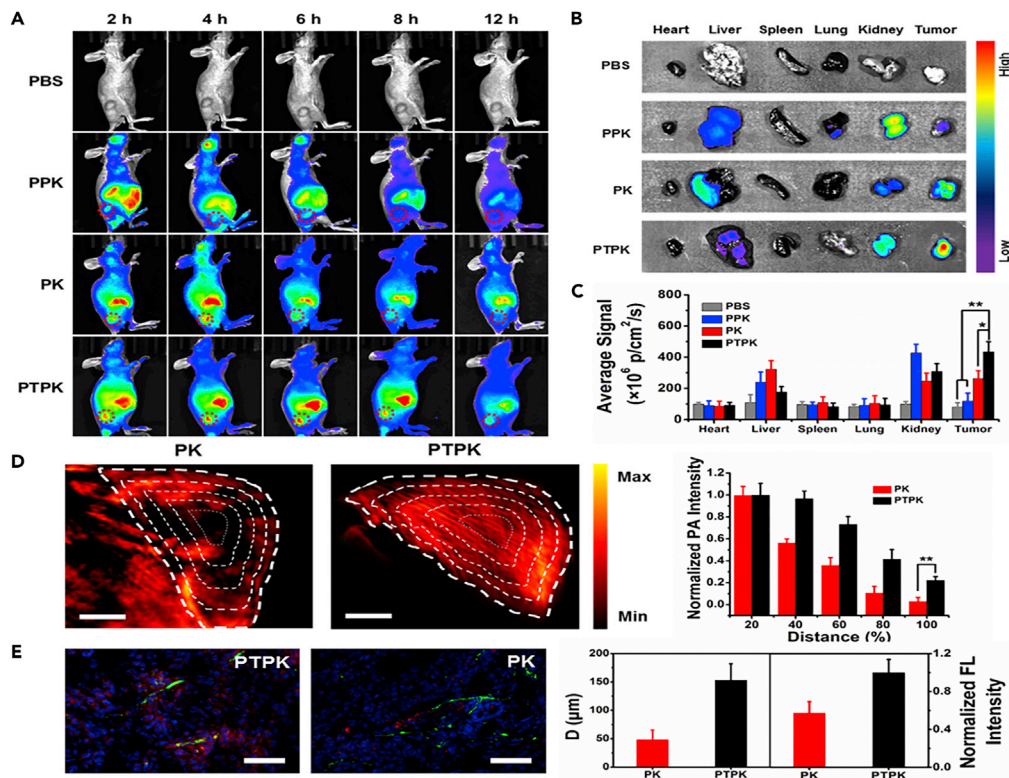
Figure 3. Tumor Accumulation and Penetration of PTPK under US Irradiation

(A) *In vivo* NIR images of the nude mice bearing Panc-1 tumors after intravenous administration of Cy5-labeled PPK, PK, and PTPK under US treatment. The red circles indicate the tumor sites.

(B) *Ex vivo* images of tumor and major organs at 12 h post injection of PPK, PK, and PTPK after US treatment.

(C) Fluorescent quantitative analysis of *ex vivo* tumor and major organs at 12 h (N = 3).

(D) *In vivo* PA imaging (left) and corresponding quantitative analysis (right) of tumors after i.v. injection of PK and PTPK. Scale bar: 2 mm.

(E) Frozen sections (left), penetration distance and fluorescent quantitative analysis (right) of Panc-1 tumors after treatment with Cy5-labeled PK or PTPK (red). The tumor vessels and nuclei are stained with FITC-tagged CD31 antibody (green) and DAPI (blue), respectively. Scale bar: 50 μm. **$p < 0.01$, *$p < 0.05$

imaging system is applied to monitor the biodistribution *in vivo* (Figure 3A). After US treatment, real-time fluorescence of PTPK in tumor is obviously stronger than that in the PPK and PK groups, and the average fluorescent intensity of mice treated with PTPK is 1.5- to 2-fold higher than those of other groups in tumor site at 6 h (Figure S11). At the same time, the tumor-bearing mice are sacrificed at 12 h post i.v. injection, and the *ex vivo* fluorescence imaging of main organs and tumors shows the high tumor accumulation of PTPK after US treatment (Figure 3B). Notably, superior to PK nanoparticles, the PTPK with single molecule state shows obvious less liver retention. The quantitative tumor fluorescence signals of mice treated with PTPK are about 1.6 and 3.6-fold higher than those in the PK and PPK groups, respectively (Figure 3C). Moreover, the pharmacokinetics of the PPCs are measured in mice, and the half-life of PTPK is similar to that of PK nanoparticles (Figure S12). Therefore, PTPK exhibits enhanced accumulation in tumor site *in vivo*, which may be attributed to the *in situ* self-assembly and the improved cellular internalization triggered by the cascade effect under US.

Besides the sonosensitizer, the P18 with outstanding photoacoustic (PA) signal can be employed for evaluating penetration capacity of PTPK in solid tumors. The particle size of control nanoparticle PK is similar or smaller to those nanoparticles described in pancreatic cancer therapy (Poon et al., 2015; Lee et al., 2013; Li et al., 2017; He et al., 2018; Lee et al., 2013; Li et al., 2017; Poon et al., 2015). After i.v. injection of PK or PTPK, the mice are placed in a multispectral optoacoustic tomography (MOST), and the PA signals in tumor cross sections are shown in Figure 3D. Compared with the PK group, PA signal distributes throughout the entire tumor in the PTPK group, especially entering into the inner center of the solid tumor, which demonstrates the high tissue penetration ability of
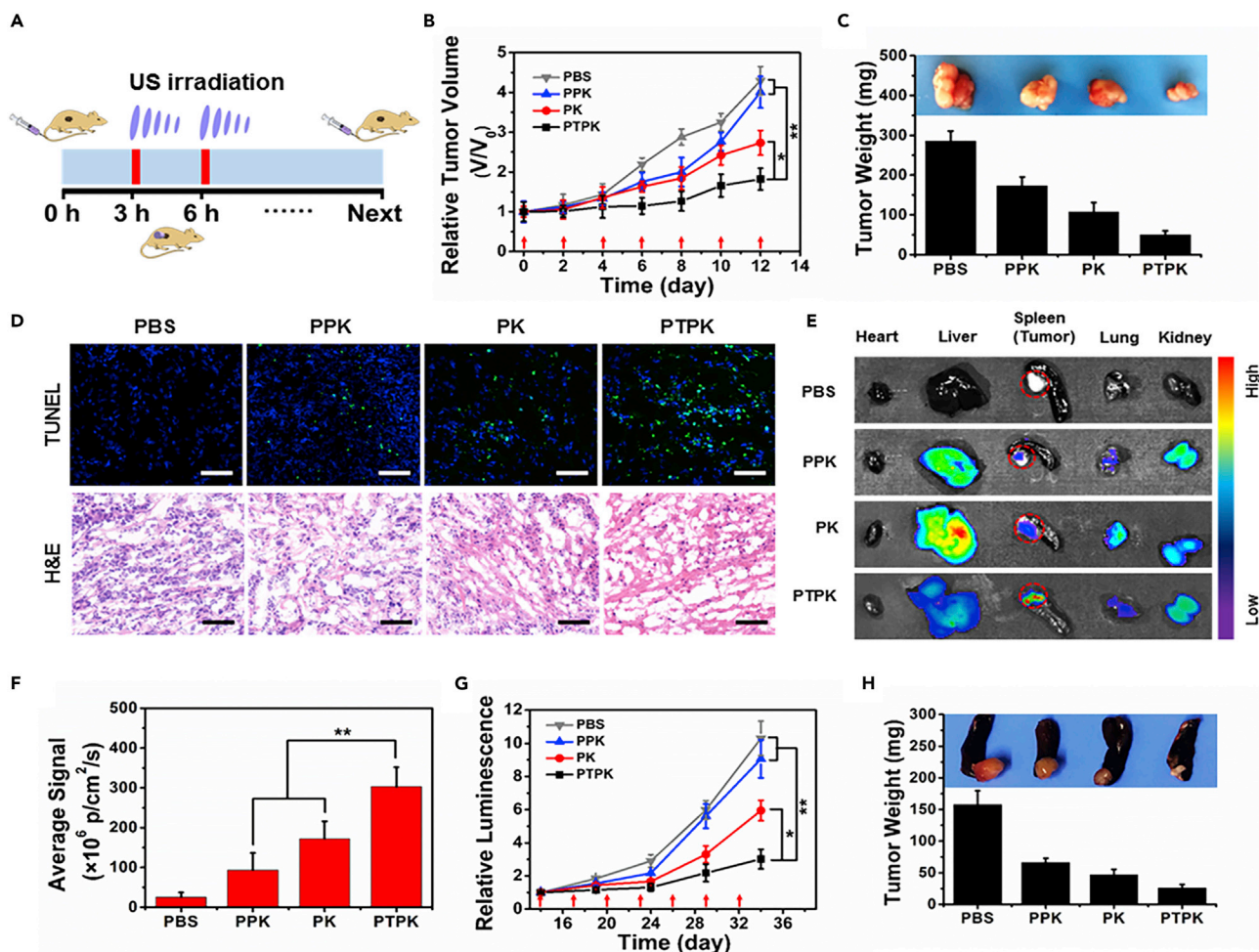
Figure 4. Tumor Inhibition Efficacy of PPCs under US Irradiation in Subcutaneous and Orthotopic Xenografts

(A) Scheme of the treatment timeline under US irradiation *in vivo*.

(B) Tumor volume changes of mice treated with PBS, PPK, PK, and PTPK after US treatment (N = 6). The red arrows indicate injections.

(C) The average tumor weight and representative tumor photographs at 12 days post treatment of PBS, PPK, PK, and PTPK (N = 6).

(D) H&E and TUNEL staining of the tumor treated by PBS, PPK, PK, and PTPK collected at 12 days over treatment course. Scale bar: 80 μm.

(E) *Ex vivo* images of orthotopic tumor and major organs at 12 h post injection of PPK, PK, PTPK, or PBS after US treatment. The red circle shows the pancreatic tumor.

(F) Fluorescent quantitative analysis of *ex vivo* orthotopic tumor at 12 h (N = 3).

(G) Quantification analysis of the *in vivo* bioluminescence signal of orthotopic tumor treated by PPK, PK, PTPK, or PBS under US. The red arrows indicate injections.

(H) The average orthotopic tumor weight and tumor photographs at 34 days post treatment of PBS, PPK, PK, and PTPK (N = 6). **p < 0.01, *p < 0.05.

single-stranded PTPK. The quantitative PA signal intensity from the tumor edge to center shows the long-lasting strong signal of PTPK, whereas PK exhibits significant signal attenuation and lower intensity, which are consistent with NIR imaging results *in vivo*. To further quantify the penetration distance of PTPK (labeled with Cy5, red signal), cryosections of solid tumor are analyzed, in which cell nuclei are stained by DAPI (blue signal) and the vessels are labeled by FITC-tagged CD31 antibody (green signal). As shown in Figure 3E, compared with PK nanoparticles, PTPK single chain can reach the tissue far away from blood vessels. Subsequently, according to the simulated scatter diagrams (Figure S13) (Liu et al., 2018), the penetration distance of PTPK group is ~153.2 ± 28.7 μm, approximately three times deeper than that of PK nanoparticles (48.3 ± 17.1 μm). Besides, the fluorescent intensity of PTPK-treated tumor is obviously stronger than that of the PK group (about 1.8-fold). All the above results indicate that the US-activated cascade effect realizes the effective penetration and accumulation of PPCs in Panc-1 solid tumor, which may inhibit tumor growth effectively *in vivo*.

Tumor Growth Inhibition under US Irradiation

The *in vivo* antitumor efficacy of PTPK is further studied using nude female mice subcutaneous and ortho-topic inoculated with Panc-1 tumor model (Figure 4A). PTPK presents the highest significant tumor inhibi-tion efficacy upon US irradiation in Panc-1 subcutaneous tumor mice model (Figure 4B). When the mice are sacrificed on the 12th day, compared with PPK and PK groups, there is considerable decrease of the tumor weights in the PTPK group, which can be attributed to the deep penetration of single chain and high inter-nalization of emerged self-assembled nanoparticles (Figure 4C). The H&E staining and TUNEL assay (Figure 4D) of tumor tissue further prove the significant apoptosis induced by PTPK, indicating the effective tumor inhibition by US-triggered cascade effect. In addition, there is no obvious change of body weight during the treatment (Figure S14) and no apparent organ damage in H&E staining of the main organs (heart, liver, spleen, lungs, and kidneys) (Figure S15), indicating negligible toxicity at the treatment dose.

US has been approved to reach a depth of above 10 cm in soft tissue, suggesting that US can be applied in orthotopic model as a practical technique in clinical translation. On this base, an orthotopic pancreatic tu-mor (inoculation of luciferase-expressing Panc-1 cells) model is established in mice to evaluate the thera-peutic effect of PPCs with US-triggered cascade process (Figure S16). Cy5-labeled PPK, PK, PTPK, or PBS is i.v. injected into Panc-1 orthotopic tumor mice, and the *ex vivo* biodistribution in major organs at 24 h is observed by fluorescence imaging (Figure 4E). After US treatment, the fluorescence intensity of the PTPK group is about 3.4- and 1.4-fold higher than that of PPK and PK groups, respectively (Figures 4F and S17), indicating specific tumor accumulation owing to the US-induced *in situ* self-assembly. For moni-toring the orthotopic tumor progression during the treatment, D-luciferin sodium salt (150 mg/kg) solution is intraperitoneally injected into the mice and *in vivo* bioluminescence imaging of the mice is performed (Figures 4G and S18). Obviously, the fluorescence from orthotopic pancreatic tumors is slightly stronger in the PTPK group after 34 days, whereas the PPK, PK, and PBS groups show significant fluorescence enhancement. Finally, the mice are sacrificed at 34 days, and the PTPK group shows the highest tumor in-hibition ratio up to 83.6% (Figure 4H) and no obvious change of body weight during the treatment (Fig-ure S19), which is consistent with the results from the subcutaneous tumor (Figure 4B). Therefore, the US-activated cascade effect of PTPK can inhibit tumor growth effectively both in subcutaneous and ortho-topic xenografts.

DISCUSSION

The US-activated cascade effect has been approved to be a substantive strategy for treatment of hypovas-cular solid tumor. The PTPK in the single-molecule state presents remarkable solid tumor penetrability. Un-der US irradiation, $^1O_2$ generated by sonosensitizer P18 induces the departure of hydrophilic PEG from PTPK, which results in self-assembly due to hydrophobic interaction. The self-assembled PK nanoparticles exhibit more effective cellular internalization assisted by US, which enhances the tumor accumulation and antitumor activity in subcutaneous pancreatic tumor-bearing mouse model. Encouragingly, taking advan-tage of high tissue-penetrating depth and spatial precision of US, PTPK leads to the effective inhibition of tumor growth in orthotopic pancreatic tumor models. This US-activated cascade strategy offers a new perspective to develop nanomaterials for precise and personalized cancer treatment. For further support-ing the advantages of this strategy, the further improvement such as combining first-line chemotherapeutic drug gemcitabine is undergoing.

Limitations of the Study

To date, this US-activated cascade strategy is only applied for peptide drug delivery. Owing to the high IC_{50} of peptide drug, the therapeutic effect *in vivo* needs to be improved. So, chemotherapeutic drugs with low IC_{50}, such as doxorubicin (DOX) and gemcitabine (Gem), should be considered as the model drug for further demonstrating the advantages of this strategy.

Resource Availability

Lead Contact

Z. Y. Qiao (qiaozy@nanoctr.cn).

Materials Availability

All the materials necessary to reproduce this study are included in the manuscript and Supplemental Information.

Data and Code Availability

The data that support the findings of this study are available from the corresponding author upon reasonable request.

METHODS

All methods can be found in the accompanying Transparent Methods supplemental file.

SUPPLEMENTAL INFORMATION

Supplemental Information can be found online at https://doi.org/10.1016/j.isci.2020.101144.

AUTHOR CONTRIBUTIONS

D.-B.C. and X.-H.Z. contributed equally to this work. D.-B.C., X.-H.Z., and Z.-Y.Q. conceived the project, are responsible for the design and experiments, and wrote the manuscript. D.-B. C. and X.-H.Z. contributed to material synthesis and characterization. D.-B.C. and Y.C. performed the *in vivo* imaging and therapeutic analysis. H.C. and H.W. analyzed and processed the results. All authors reviewed the manuscript.

DECLARATION OF INTERESTS

The authors declare no competing interests.

REFERENCES

Blanco, E., Shen, H., and Ferrari, M. (2015). Principles of nanoparticle design for overcoming biological barriers to drug delivery. Nat. Biotechnol. *33*, 941–951.

Blum, A.P., Kammeyer, J.K., Rush, A.M., Callmann, C.E., Hahn, M.E., and Gianneschi, N.C. (2015). Stimuli-responsive nanomaterials for biomedical applications. J. Am. Chem. Soc. *137*, 2140–2154.

Celli, J.P., Spring, B.Q., Rizvi, I., Evans, C.L., Samkoe, K.S., Verma, S., Pogue, B.W., and Hasan, T. (2010). Imaging and photodynamic therapy: mechanisms, monitoring, and optimization. Chem. Rev. *110*, 2795–2838.

Cheng, D.B., Qi, G.B., Wang, J.Q., Cong, Y., Liu, F.H., Yu, H., Qiao, Z.Y., and Wang, H. (2017). In situ monitoring intracellular structural change of nanovehicles through photoacoustic signals based on phenylboronate-linked RGD-dextran/purpurin 18 conjugates. Biomacromolecules *18*, 1249–1258.

Cheng, D.B., Zhang, X.H., Gao, Y.J., Ji, L., Hou, D., Wang, Z., Xu, W., Qiao, Z.Y., and Wang, H. (2019). Endogenous reactive oxygen species-triggered morphology transformation for enhanced cooperative interaction with mitochondria. J. Am. Chem. Soc. *141*, 7235–7239.

Cong, Y., Ji, L., Gao, Y.J., Liu, F.H., Cheng, D.B., Hu, Z., Qiao, Z.Y., and Wang, H. (2019). Microenvironment-induced in situ self-assembly of polymer-peptide conjugates that attack solid tumors deeply. Angew. Chem. Int. Ed. *58*, 4632–4637.

Deepagan, V.G., You, D.G., Um, W., Ko, H., Kwon, S., Choi, K.Y., Yi, G.R., Lee, J.Y., Lee, D.S., Kim, K., et al. (2016). Long-circulating Au-TiO2 nanocomposite as a sonosensitizer for ROS-mediated eradication of cancer. Nano Lett. *16*, 6257–6264.

Dehaini, D., Fang, R.H., Luk, B.T., Pang, Z., Hu, C.M., Kroll, A.V., Yu, C.L., Gao, W., and Zhang, L. (2016). Ultra-small lipid-polymer hybrid nanoparticles for tumor-penetrating drug delivery. Nanoscale *8*, 14411–14419.

Elgogary, A., Xu, Q., Poore, B., Alt, J., Zimmermann, S.C., Zhao, L., Fu, J., Chen, B., Xia, S., Liu, Y., et al. (2016). Combination therapy with BPTES nanoparticles and metformin targets the metabolic heterogeneity of pancreatic cancer. Proc. Natl. Acad. Sci. U S A *113*, E5328–E5336.

Gao, S., Wang, G., Qin, Z., Wang, X., Zhao, G., Ma, Q., and Zhu, L. (2017). Oxygen-generating hybrid nanoparticles to enhance fluorescent/photoacoustic/ultrasound imaging guided tumor photodynamic therapy. Biomaterials *112*, 324–335.

Gonzales, J., Nair, R.K., Madsen, S.J., Krasieva, T., and Hirschberg, H. (2016). Focused ultrasound-mediated sonochemical internalization: an alternative to light-based therapies. J. Biomed. Opt. *21*, 78002.

Guan, X., Guo, Z., Lin, L., Chen, J., Tian, H., and Chen, X. (2016). Ultrasensitive pH triggered charge/size dual-rebound gene delivery system. Nano Lett. *16*, 6823–6831.

Halbrook, C.J., and Lyssiotis, C.A. (2017). Employing metabolism to improve the diagnosis and treatment of pancreatic cancer. Cancer Cell *31*, 5–19.

Han, X., Li, Y., Xu, Y., Zhao, X., Zhang, Y., Yang, X., Wang, Y., Zhao, R., Anderson, G.J., Zhao, Y., and Nie, G. (2018). Reversal of pancreatic desmoplasia by re-educating stellate cells with a tumour microenvironment-activated nanosystem. Nat. Commun. *9*, 3390.

He, X., Chen, X., Liu, L., Zhang, Y., Lu, Y., Zhang, Y., Chen, Q., Ruan, C., Guo, Q., Li, C., et al. (2018). Sequentially triggered nanoparticles with tumor penetration and intelligent drug release for pancreatic cancer therapy. Adv. Sci. *5*, 1701070.

He, Y., Wan, J., Yang, Y., Yuan, P., Yang, C., Wang, Z., and Zhang, L. (2019). Multifunctional polypyrrole-coated mesoporous TiO2 nanocomposites for photothermal,

sonodynamic, and chemotherapeutic treatments and dual-modal ultrasound/photoacoustic imaging of tumors. Adv. Healthc. Mater. *8*, e1801254.

Hida, K., Maishi, N., Sakurai, Y., Hida, Y., and Harashima, H. (2016). Heterogeneity of tumor endothelial cells and drug delivery. Adv. Drug Deliv. Rev. *99*, 140–147.

Huang, P., Qian, X., Chen, Y., Yu, L., Lin, H., Wang, L., Zhu, Y., and Shi, J. (2017). Metalloporphyrin-encapsulated biodegradable nanosystems for highly efficient magnetic resonance imaging-guided sonodynamic cancer therapy. J. Am. Chem. Soc. *139*, 1275–1284.

Ji, C., Gao, Q., Dong, X., Yin, W., Gu, Z., Gan, Z., Zhao, Y., and Yin, M. (2018). A size-reducible nanodrug with an aggregation-enhanced photodynamic effect for deep chemo-photodynamic therapy. Angew. Chem. Int. Ed. *57*, 11384–11388.

Junttila, M.R., and de Sauvage, F.J. (2013). Influence of tumour micro-environment heterogeneity on therapeutic response. Nature *501*, 346–354.

Lee, G.Y., Qian, W.P., Wang, L., Wang, Y.A., Staley, C.A., Satpathy, M., Nie, S., Mao, H., and Yang, L. (2013). Theranostic nanoparticles with controlled release of gemcitabine for targeted therapy and MRI of pancreatic cancer. ACS Nano *7*, 2078–2089.

Li, L.L., Zeng, Q., Liu, W.J., Hu, X.F., Li, Y., Pan, J., Wan, D., and Wang, H. (2016a). Quantitative analysis of caspase-1 activity in living cells through dynamic equilibrium of chlorophyll-based nano-assembly modulated photoacoustic signals. ACS Appl. Mater. Interfaces *8*, 17936–17943.

Li, W.P., Su, C.H., Chang, Y.C., Lin, Y.J., and Yeh, C.S. (2016b). Ultrasound-induced reactive oxygen species mediated therapy and imaging using a fenton reaction activable polymersome. ACS Nano *10*, 2017–2027.

Li, Y., Wang, H., Wang, K., Hu, Q., Yao, Q., Shen, Y., Yu, G., and Tang, G. (2017). Targeted Co-delivery of PTX and TR3 siRNA by PTP peptide modified dendrimer for the treatment of pancreatic cancer. Small *13*, 1602697.

Lin, X., Liu, S., Zhang, X., Zhu, R., Chen, S., Chen, X., Song, J., and Yang, H. (2020). An ultrasound activated vesicle of janus Au-MnO nanoparticles for promoted tumor penetration and sono-chemodynamic therapy of orthotopic liver cancer. Angew. Chem. Int. Ed. *59*, 1682–1688.

Liu, F.H., Cong, Y., Qi, G.B., Ji, L., Qiao, Z.Y., and Wang, H. (2018). Near-infrared laser-driven in situ self-assembly as a general strategy for deep tumor therapy. Nano Lett. *18*, 6577–6584.

Liu, J., Jin, C., Yuan, B., Chen, Y., Liu, X., Ji, L., and Chao, H. (2017). Enhanced cancer therapy by the marriage of metabolic alteration and mitochondrial-targeted photodynamic therapy using cyclometalated Ir(iii) complexes. Chem. Commun. (Camb.) *53*, 9878–9881.

Liu, X., Chen, Y., Li, H., Huang, N., Jin, Q., Ren, K., and Ji, J. (2013). Enhanced retention and cellular uptake of nanoparticles in tumors by controlling their aggregation behavior. ACS Nano *7*, 6244–6257.

Matsumoto, Y., Nichols, J.W., Toh, K., Nomoto, T., Cabral, H., Miura, Y., Christie, R.J., Yamada, N., Ogura, T., Kano, M.R., et al. (2016). Vascular bursts enhance permeability of tumour blood vessels and improve nanoparticle delivery. Nat. Nanotechnol. *11*, 533–538.

McEwan, C., Owen, J., Stride, E., Fowley, C., Nesbitt, H., Cochrane, D., Coussios, C.C., Borden, M., Nomikou, N., McHale, A.P., and Callan, J.F. (2015). Oxygen carrying microbubbles for enhanced sonodynamic therapy of hypoxic tumours. J. Control Release *203*, 51–56.

Meng, Z., Wei, F., Wang, R., Xia, M., Chen, Z., Wang, H., and Zhu, M. (2016). NIR-Laser-Switched in vivo smart nanocapsules for synergic photothermal and chemotherapy of tumors. Adv. Mater. *28*, 245–253.

Min, H.S., Son, S., You, D.G., Lee, T.W., Lee, J., Lee, S., Yhee, J.Y., Lee, J., Han, M.H., Park, J.H., et al. (2016). Chemical gas-generating nanoparticles for tumor-targeted ultrasound imaging and ultrasound-triggered drug delivery. Biomaterials *108*, 57–70.

Nomikou, N., Curtis, K., McEwan, C., O'Hagan, B.M.G., Callan, B., Callan, J.F., and McHale, A.P. (2017). A versatile, stimulus-responsive nanoparticle-based platform for use in both sonodynamic and photodynamic cancer therapy. Acta Biomater. *49*, 414–421.

Peng, C., Xu, J., Yu, M., Ning, X., Huang, Y., Du, B., Hernandez, E., Kapur, P., Hsieh, J.T., and Zheng, J. (2019). Tuning the in vivo transport of anticancer drugs using renal-clearable gold nanoparticles. Angew. Chem. Int. Ed. *58*, 8479–8483.

Poon, C., He, C., Liu, D., Lu, K., and Lin, W. (2015). Self-assembled nanoscale coordination polymers carrying oxaliplatin and gemcitabine for synergistic combination therapy of pancreatic cancer. J. Control Release *201*, 90–99.

Qian, X., Zheng, Y., and Chen, Y. (2016). Micro/nanoparticle-augmented sonodynamic therapy (SDT): breaking the depth shallow of photoactivation. Adv. Mater. *28*, 8097–8129.

Rosenblum, D., Joshi, N., Tao, W., Karp, J.M., and Peer, D. (2018). Progress and challenges towards targeted delivery of cancer therapeutics. Nat. Commun. *9*, 1410.

Song, X., Feng, L., Liang, C., Yang, K., and Liu, Z. (2016). Ultrasound triggered tumor oxygenation with oxygen-shuttle nanoperfluorocarbon to overcome hypoxia-associated resistance in cancer therapies. Nano Lett. *16*, 6145–6153.

Sun, Q., Zhou, Z., Qiu, N., and Shen, Y. (2017). Rational design of cancer nanomedicine: nanoproperty integration and synchronization. Adv. Mater. *29*, 1606628.

Tao, Z., Muzumdar, M.D., Detappe, A., Huang, X., Xu, E.S., Yu, Y., Mouhieddine, T.H., Song, H., Jacks, T., and Ghoroghchian, P.P. (2018). Differences in nanoparticle uptake in transplanted and autochthonous models of pancreatic cancer. Nano Lett. *18*, 2195–2208.

Vankayala, R., and Hwang, K.C. (2018). Near-infrared-light-activatable nanomaterial-mediated phototheranostic nanomedicines: an emerging paradigm for cancer treatment. Adv. Mater. *30*, e1706320.

Wang, S., Huang, P., and Chen, X. (2016). Hierarchical targeting strategy for enhanced tumor tissue accumulation/retention and cellular internalization. Adv. Mater. *28*, 7340–7364.

Wu, P., Sun, Y., Dong, W., Zhou, H., Guo, S., Zhang, L., Wang, X., Wan, M., and Zong, Y. (2019). Enhanced anti-tumor efficacy of hyaluronic acid modified nanocomposites combined with sonochemotherapy against subcutaneous and metastatic breast tumors. Nanoscale *11*, 11470–11483.

Yang, R., An, J., Zhu, H., Yan, X., and Gao, H. (2019). Multipronged design of theranostic nanovehicles with endogenous and exogenous stimuli-responsiveness for precise cancer therapy. J. Mater. Chem. B *7*, 1160–1166.

Yuan, Y., Liu, J., and Liu, B. (2014). Conjugated-polyelectrolyte-based polyprodrug: targeted and image-guided photodynamic and chemotherapy with on-demand drug release upon irradiation with a single light source. Angew. Chem. Int. Ed. *53*, 7163–7168.

Yuan, Y., Zhang, C.J., Xu, S., and Liu, B. (2016). A self-reporting AIE probe with a built-in singlet oxygen sensor for targeted photodynamic ablation of cancer cells. Chem. Sci. *7*, 1862–1866.

Zhang, D., Qi, G.B., Zhao, Y.X., Qiao, S.L., Yang, C., and Wang, H. (2015). In situ formation of nanofibers from purpurin18-peptide conjugates and the assembly induced retention effect in tumor sites. Adv. Mater. *27*, 6125–6130.

Zhang, W., Hu, X., Shen, Q., and Xing, D. (2019). Mitochondria-specific drug release and reactive oxygen species burst induced by polyprodrug nanoreactors can enhance chemotherapy. Nat. Commun. *10*, 1704.

Zhang, Y., Cai, K., Li, C., Guo, Q., Chen, Q., He, X., Liu, L., Zhang, Y., Lu, Y., Chen, X., et al. (2018). Macrophage-membrane-coated nanoparticles for tumor-targeted chemotherapy. Nano Lett. *18*, 1908–1915.

Zhang, Z., Ma, R., and Shi, L. (2014). Cooperative macromolecular self-assembly toward polymeric assemblies with multiple and bioactive functions. Acc. Chem. Res. *47*, 1426–1437.

Zheng, D.W., Li, B., Li, C.X., Fan, J.X., Lei, Q., Li, C., Xu, Z., and Zhang, X.Z. (2016). Carbon-dot-decorated carbon nitride nanoparticles for enhanced photodynamic therapy against hypoxic tumor via water splitting. ACS Nano *10*, 8715–8722.

Zhu, L., Staley, C., Kooby, D., El-Rays, B., Mao, H., and Yang, L. (2017). Current status of biomarker and targeted nanoparticle development: the precision oncology approach for pancreatic cancer therapy. Cancer Lett. *388*, 139–148.

Supplemental Information

Ultrasound-Activated Cascade Effect

for Synergistic Orthotopic

Pancreatic Cancer Therapy

Dong-Bing Cheng, Xue-Hao Zhang, Yuanfang Chen, Hao Chen, Zeng-Ying Qiao, and Hao Wang
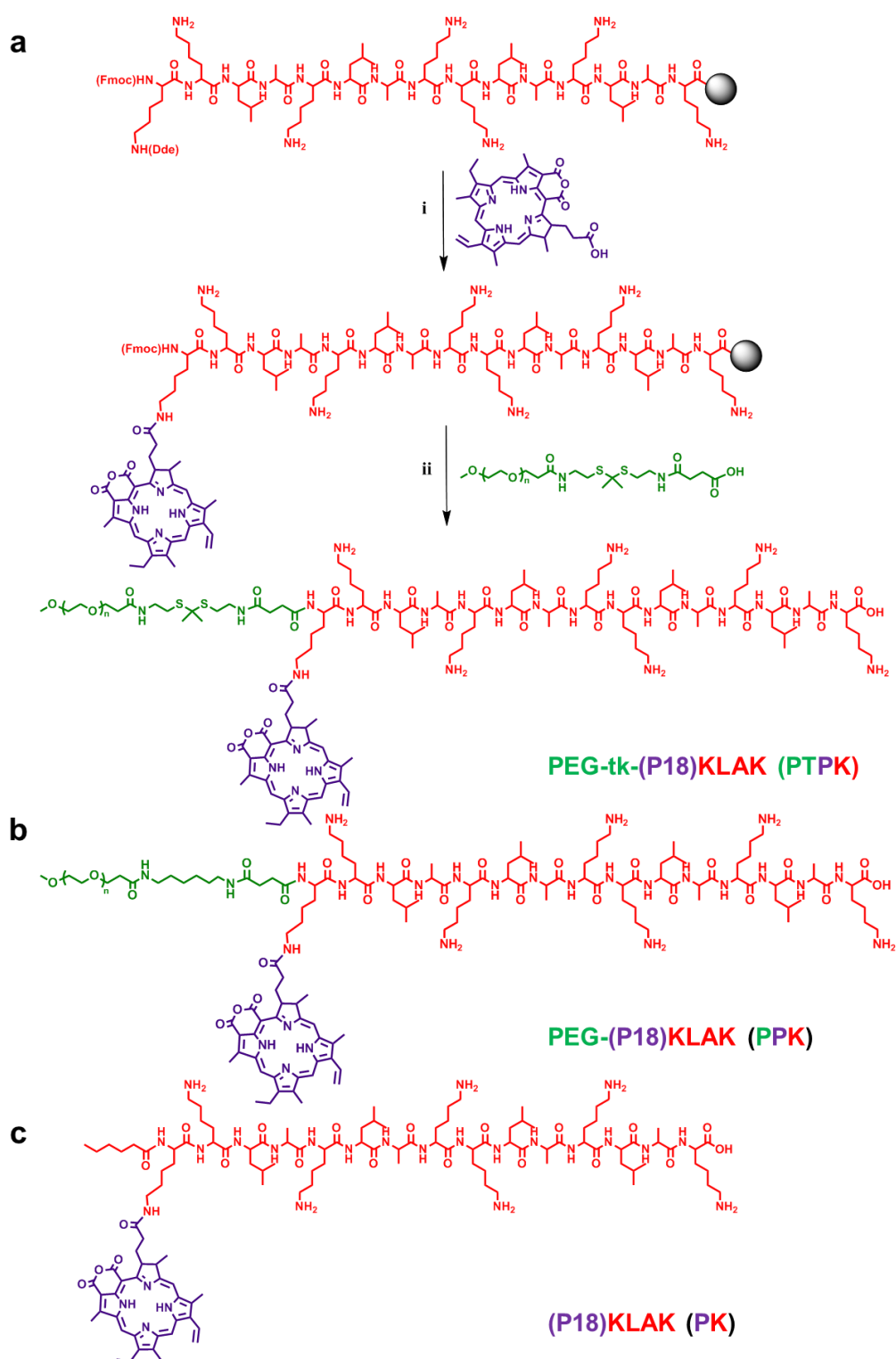
Scheme S1. (a) Synthesis of PTPK. i) 2% DBU,DMF; P18, NMM, *N*-HBTU, DMF, 3 h. ii) 2% Hydrazine hydrate, DMF; PEG, NMM, *N*-HBTU, DMF, 6 h. (b) Molecular structure of PPK. (c) Molecular structure of PK. Related to Figure 1.
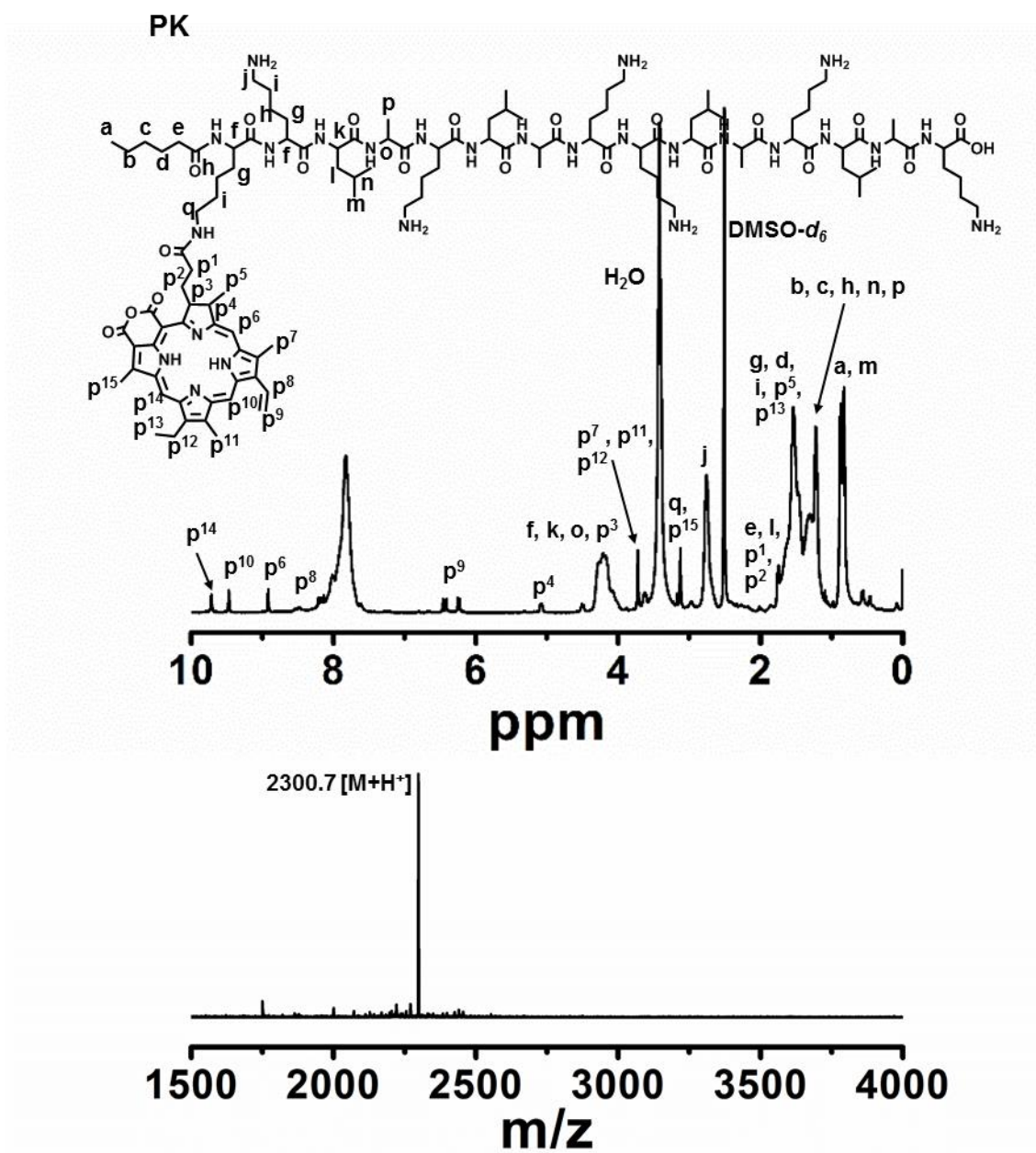
Figure S1. ^{1}H NMR (400 MHz, DMSO-d_6) and MALDI-TOF-MS spectra of PK. Related to Figure 1.
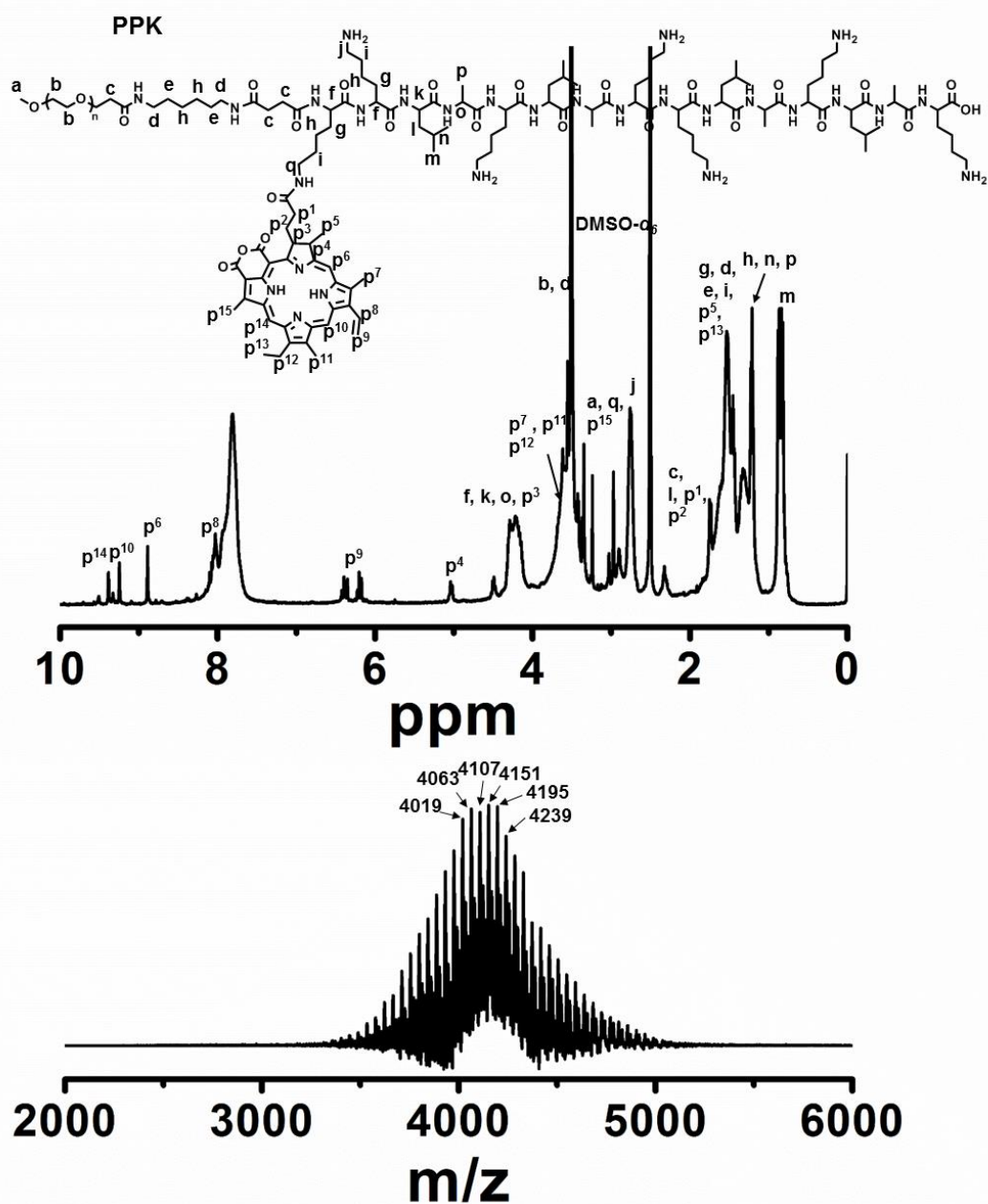
Figure S2. ^{1}H NMR (400 MHz, DMSO-d_6) and MALDI-TOF-MS spectra of PPK. Related to Figure 1.
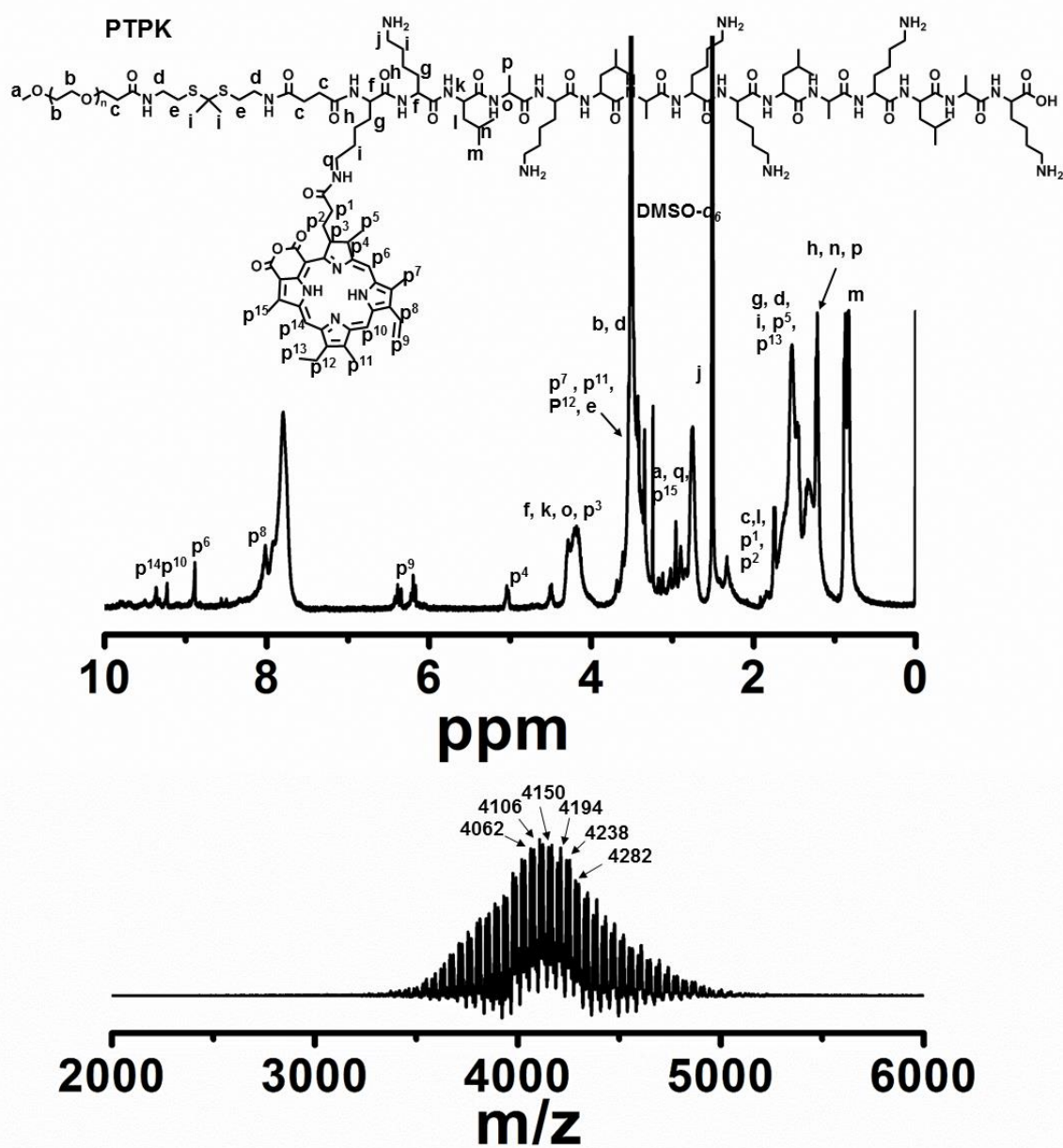
Figure S3. ^{1}H NMR (400 MHz, DMSO-d_6) and MALDI-TOF-MS spectra of PTPK. Related to Figure 1.
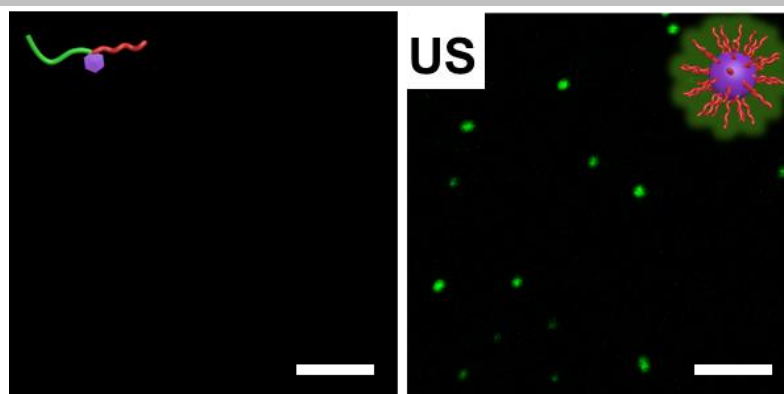
Figure S4. CLSM images of DBD-labeled PTPK (10 μM) with or without US treatment (PB, 0.01 M, pH 7.4). Scale bar: 2 μm. Related to Figure 1.
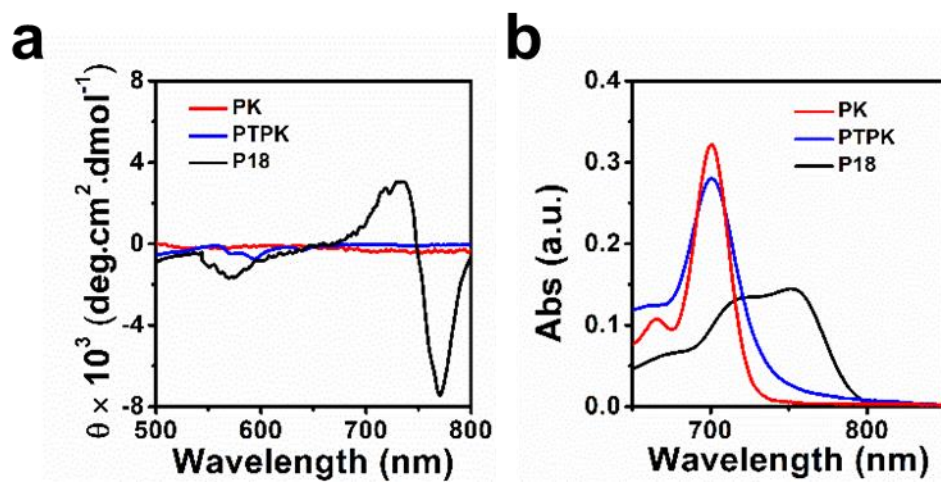
Figure S5. a) CD spectra of PTPK, PK and P18. b) UV−vis spectra of PTPK, PK and P18 in PB (0.01 M, pH 7.4). Related to Figure 1.
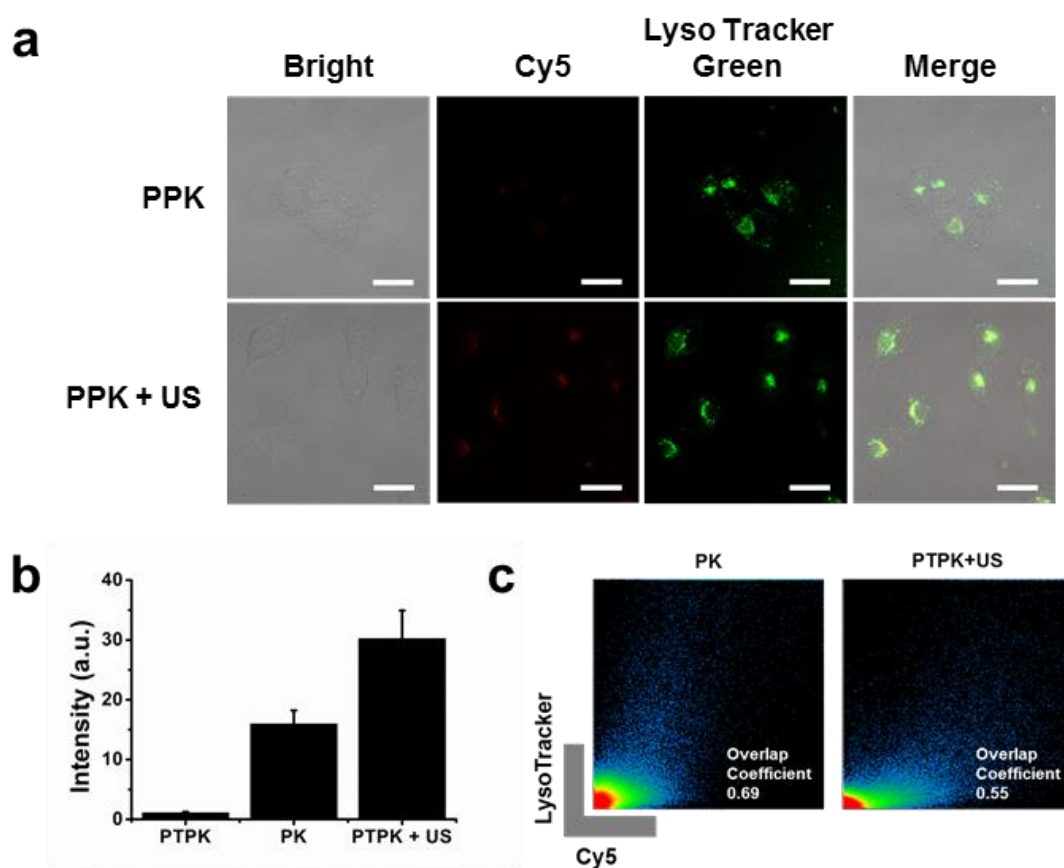
Figure S6. a) CLSM images of Panc-1 cells treated with Cy5-labeled PPK (10 μM for KLAK) with or without US treatment within 4 h. Cy5 (red): 633 nm, Lysotracker (green): 488 nm. Scale bar: 20 μm. b) The average intensity of Cy 5 fluorescence signal of cells in Figure 2a . Values are expressed as means ± S.D. (N = 3). c) Corresponding colocalization analysis of cells in Figure 2a. Related to Figure 2.
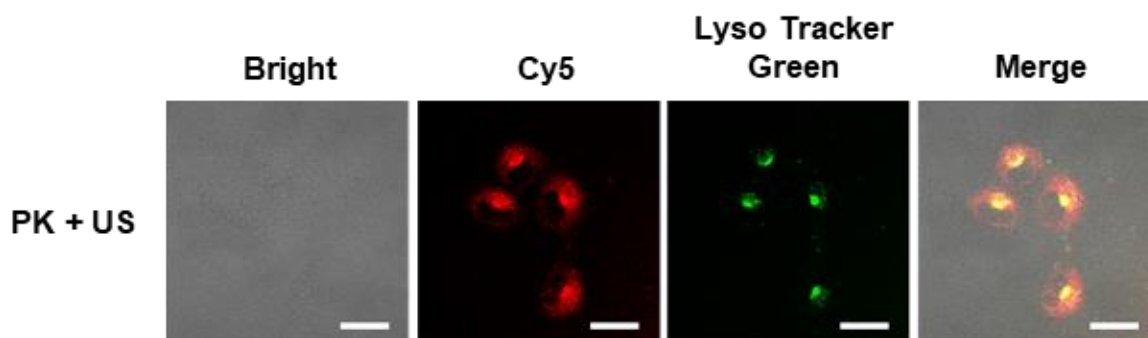
Figure S7. CLSM images of Panc-1 cells treated with Cy5-labeled PK (10 μM for KLAK) with US treatment within 4 h. Cy5 (red): 633 nm, Lysotracker (green): 488 nm. Scale bar: 20 μm. Related to Figure 2.
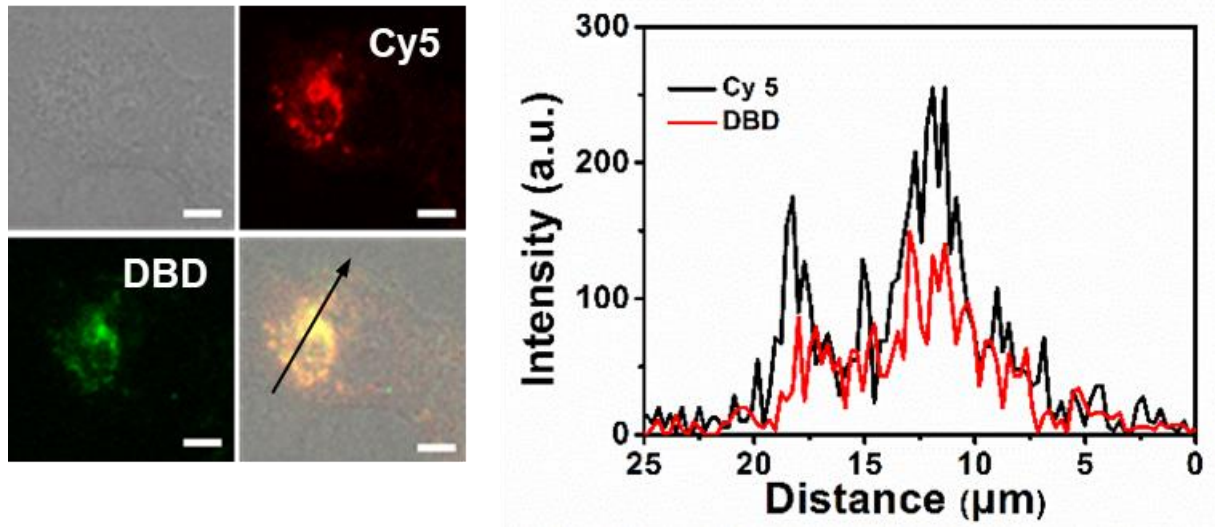
Figure S8. CLSM images (left) and corresponding quantitative fluorescence analysis in the drawing line (right) of Panc-1cells treated by double labeled PTPK under US irradiation. Scale bar: 5 μm. Related to Figure 2.
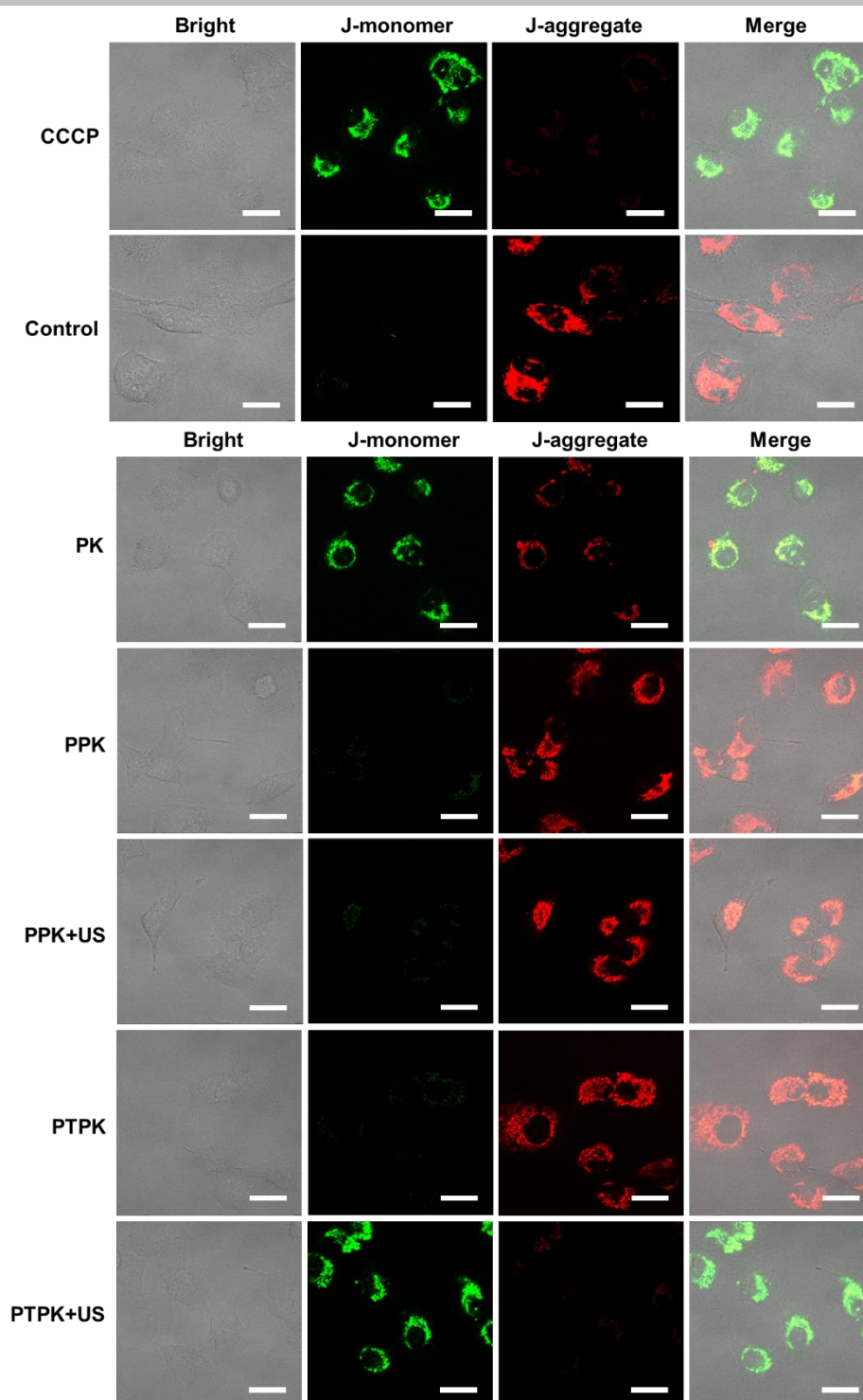
Figure S9. CLSM images with the JC-1 assay of Panc-1 cells incubated with PK, PPK and PTPK with or without US treatment for 12 h. KLAK concentration: 10 μM. Scale bar: 20 μm. Related to Figure 2.
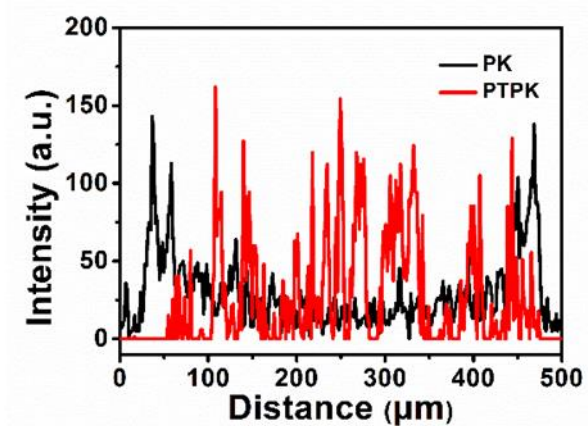
Figure S10. Quantitative fluorescence analysis in the drawing line of MCS in Figure 2d. Related to Figure 2.
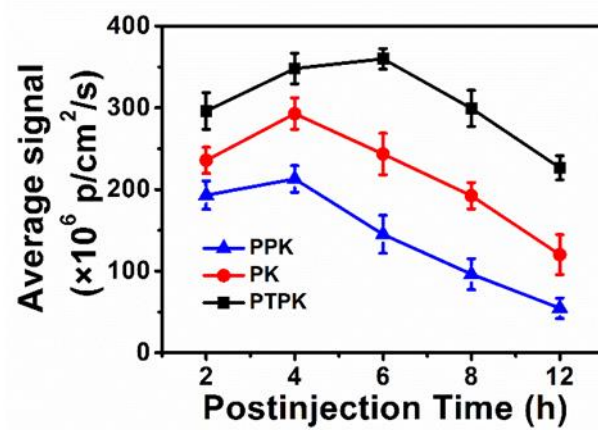
Figure S11. Quantitative fluorescence analysis in tumor at different times (N = 3). Related to Figure 3.
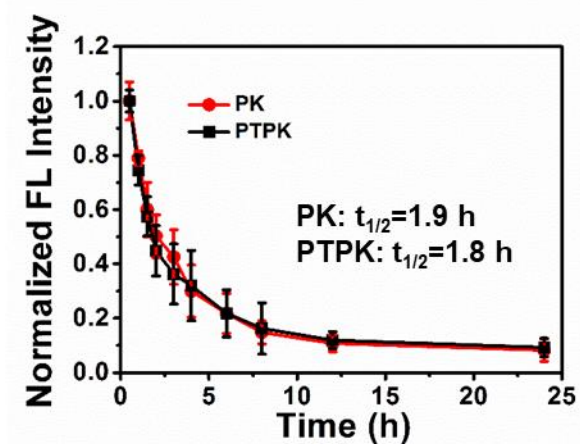
Figure S12. Normalized FL of the blood collected at different times after tail-vein injection of Cy5-labeled PPCs. Related to Figure 3.
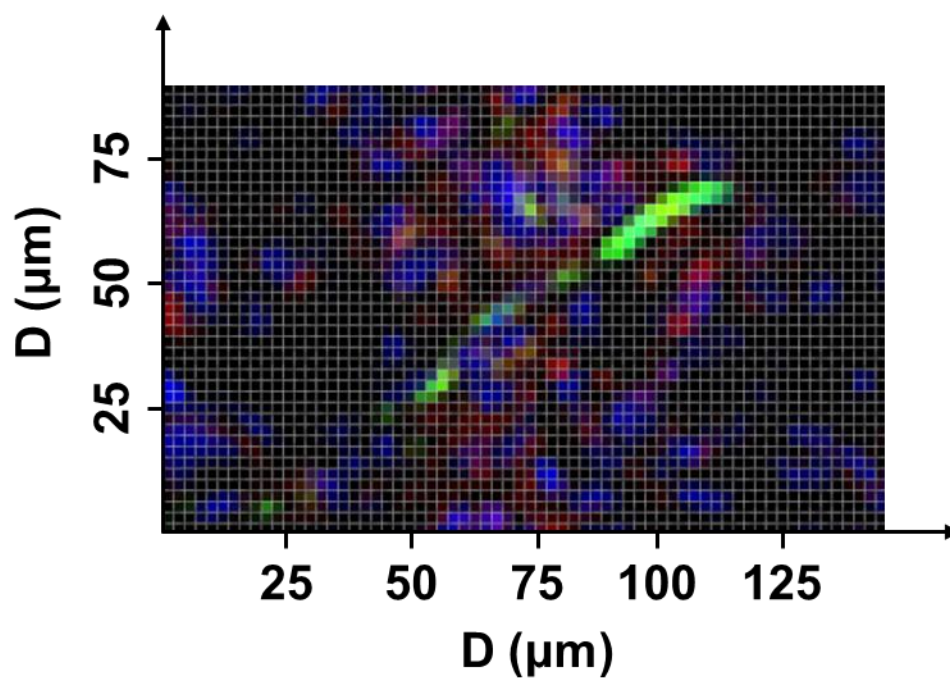
Figure S13. Method of pixel calculation for measurement of penetration distance. Related to Figure 3.
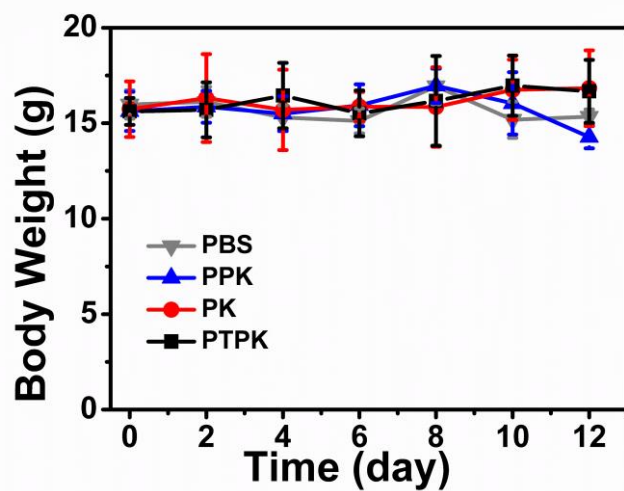
Figure S14. Body weight changes of four groups after treatment (N = 6). Related to Figure 4.
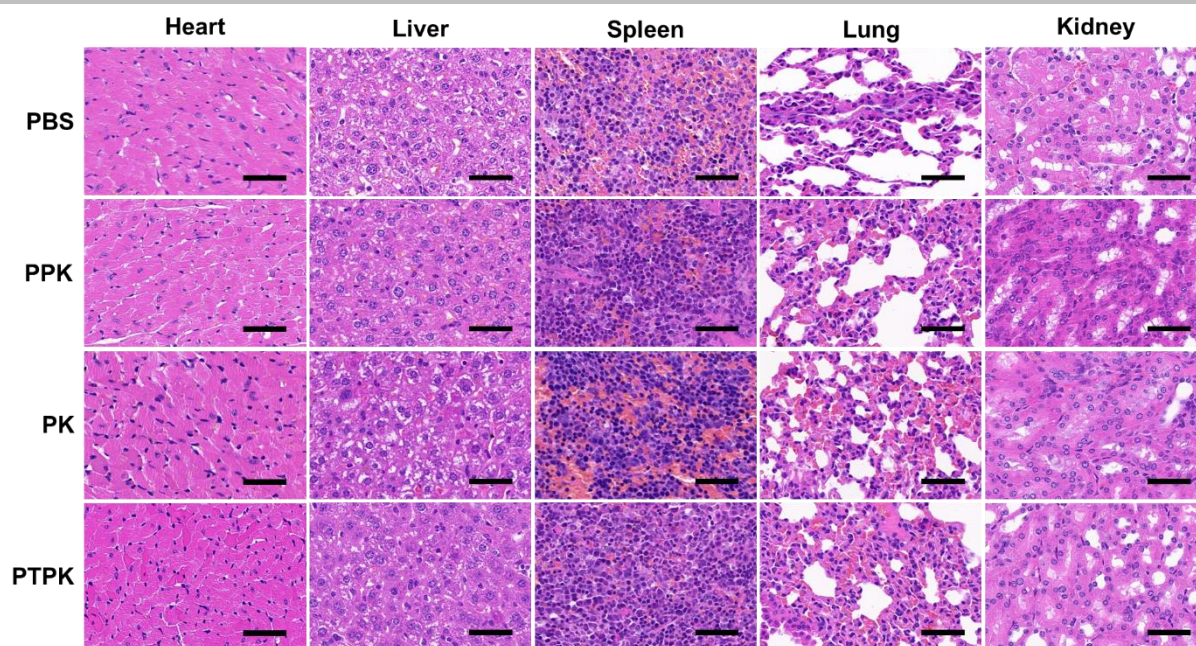
Figure S15. H&E staining of tissues (heart, liver, spleen, lung, and kidney) collected at 12 d over treatment course. Scale bar: 50 μm. Related to Figure 4.
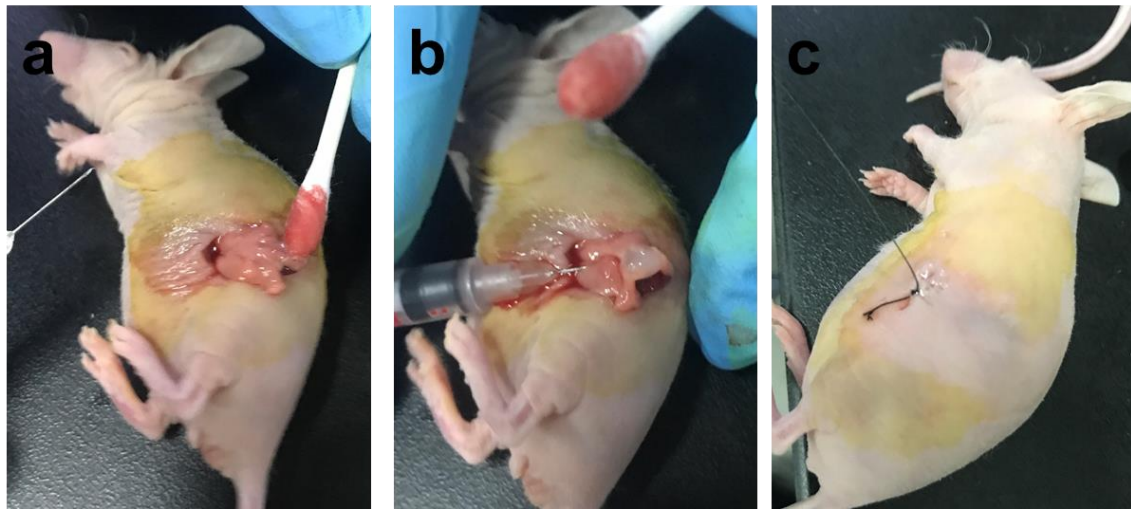
Figure S16. The process of establishment of orthotopic pancreatic tumor mouse model. a) The pancreas of mice is exposed in vitro through surgery. (b) Panc-1-luc cells are injected into the pancreas head of mice. (c) Pancreas contained with Panc-1-luc cells is embedded and the incision is sutured. Related to Figure 4.
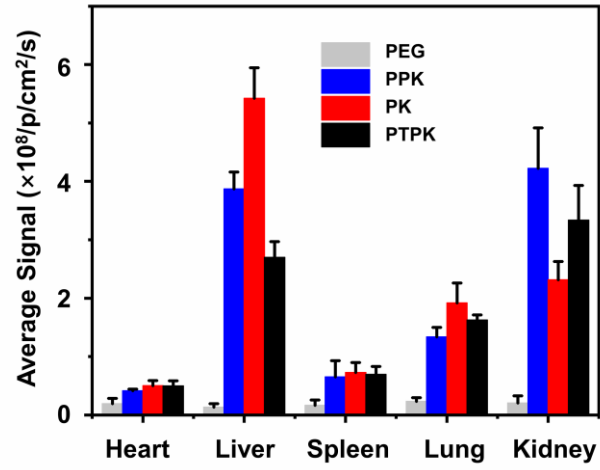
Figure S17. Fluorescent quantitative analysis of ex vivo major organs at 12 h (N = 3). Related to Figure 4.
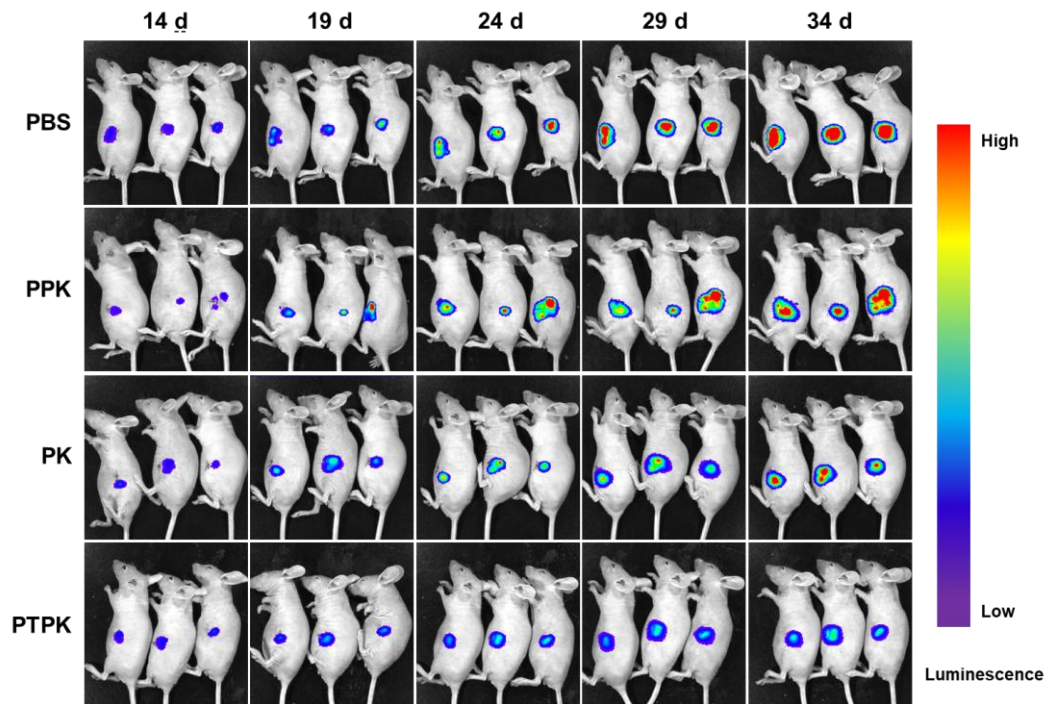
Figure S18. In vivo representative whole-body bioluminescence images of mice on days 14, 19, 24, 29 and 34. Related to Figure 4.
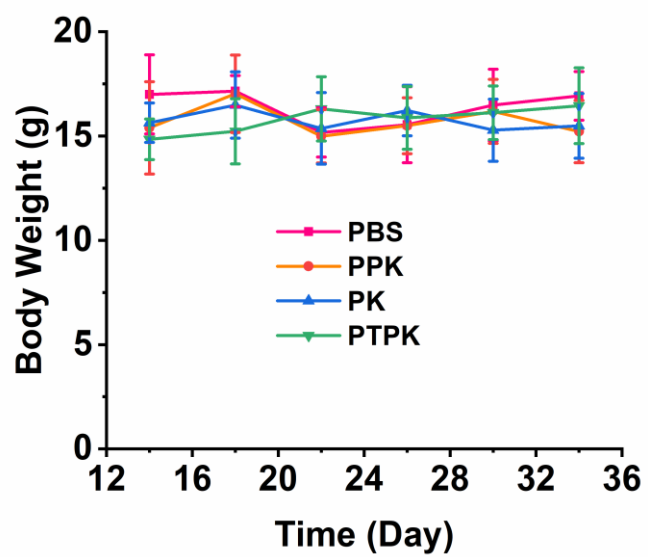
Figure S19. Body weight changes of four groups after treatment (N = 6). Related to Figure 4.

Transparent Methods

Materials.

Methoxy poly(ethylene glycol) NHS ester (mPEG, Mn = 2000), 4-(2-aminoethylamino)-7-(N, N-dimethylsulfamoyl) benzofurazan (DBD-ED) and Cy5-NHS ester are purchased from Sigma-Aldrich Chemical Co., Ltd. Purpurin-18 (P18) is obtained from Shanghai Xianhui Pharmaceutical Co., Ltd. mPEG-tk-COOH and mPEG-COOH are synthesized according previous report (Cheng et al., 2019). Phosphate-buffered saline (PBS), fetal bovine serum (FBS), DMEM (Dulbecco's modified Eagle medium) medium and Trypsin are obtained from HyClone/Thermofisher (Beijing, China). Human pancreatic Panc-1 cell line and Panc-1 cells transfected with luciferase gene (Panc-1-luc cells) are obtained from the cell culture center of the Institute of Basic Medical Sciences, Chinese Academy of Medical Sciences (Beijing, China). Lysotracker Green, JC-1 assay, and CCK-8 (cell counting kit-8) is purchased from Beyotime Institute of Biothechnology (Shanghai, China). Female BALB/c nude mice (6-8 weeks, 16-17 g) are purchased from Vital River laboratory animal technology Co., Ltd. (Beijing, China). All the other solvents used in the research are of analytical grade and used as received.

Synthesis of PEG-tk-(P18)KLAK (PTPK), PEG-(P18)KLAK (PPK) and (P18)KLAK (PK).

The conjugate PTPK is prepared by standard Fmoc solid-phase peptide synthesis. Briefly, the Lys resin (loading: 0.38 mM/g) is used for the phase supports, then repeated deprotection (piperidine: 20% v/v) and acrylation (NMM: 4%, HBTU: 6%) in anhydrous DMF. After deprotection of the Fmoc of last amino acid, mPEG-tk-COOH is dissolved in DMF (NMM: 4%) and further reacts with the peptide. The PTPK is cleaved from resin with the mixture of TFA, TIPS and H_2O in the volume ratio of 95 : 2.5 : 2.5 for 2.5 h. The final solution is concentrated, precipitated in ether and purified by reverse-phase high-performance liquid chromatography (HPLC). The PPK and PK are synthesized by the same method as above.

Preparation of the Cy5-labeled, DBD-labeled and double-labeled conjugates.

Conjugate (10 µmol) is dissolved in 2mL of $NaHCO_3$ solution (pH 8.3), then 10 µL of Cy5-NHS solution (1 mg mL^{-1}, in PB 0.01 M) is added, and the mixture is kept stirring and reacting in dark overnight. The solution is dialyzed against PB (MWCO: 1000 Da) for 24 h to gain Cy5-labeled conjugate solution. The DBD-labeled conjugate is obtained by above synthesized method, and DBD-ED is pretreated with succinic anhydride. Both Cy5 and DBD are labeled on conjugate to acquire the double-labeled conjugate.

Particle size and morphology characterization.

Nano-ZS 3600 (Malvern Instruments, UK) is used to measure the size distribution of the conjugate solutions. The conjugate solutions (10 µM) are treated with or without US irradiation before measurements. An average value is determined by three repeated measurements at 25 °C for each sample. Besides, transmission electron microscopy (TEM, Tecnai G2 20 S-TWIN) is conducted to observe the morphology and diameters of conjugates in aqueous solution, The conjugates (50 µL, 10 µM) are kept in PB solution with or without US irradiation, which are dropped on copper meshes. After 5 min, unnecessary liquid is removed and the uranyl acetate solution (10 µL) is dropped on this copper mesh to stain the samples for 10 min. Finally, the copper meshes are washed with deionized water, and dried at room temperature for observation.

$^1O_2$ Detection by electron spin resonance (ESR) spectrometer and DPBF assay.

The generation of $^1O_2$ is determined by the Bruker EMX ESR spectrometer. Typically, conjugates (10 µM) are exposed to US irradiation (1.0 MHz, 1.5 W/cm^2, 50% duty cycle) for 3 min in the presence of 2,2,6,6-Tetramethylpiperidine (TEMP, 97 µM). The $^1O_2$ signal is immediately detected by the ESR spectrometer. The amount of $^1O_2$ is measured by using 1,3-diphenylisobenzofuran (DPBF) as an indicator that following the loss of UV absorbance of DPBF in the conjugate solution. Briefly, DPBF (50 µL, 5×10^{-5} M) and fresh conjugate solution (10 µM) are mixed with 3 ml DMSO, and then the solution is exposed to US irradiation. The UV absorption at 410 nm (λ max of DPBF) is recorded every 1 min to monitor the consumption of DPBF.

Bio-TEM observation.

The treated cells are fixed overnight in 3 % glutaraldehyde. After 24 h, the samples are washed with PB solution (PB, 0.01 M) three times, and further fixed with 1 % osmium-containing PB for 2 h. Then, wash with PB solution, and the samples are dehydrated with a graded series of alcohol (50, 70, 80, 90, 100, 100, 100 %) for 10 min, alcohol/acetone mixture (1:1) for 10min, acetone twice for 10 min. Subsequently, acetone/EPON 812 resin mixtures (1:1, 1:2) are used for infiltration for 1 h, and samples are immersed in pure resin at 4 °C overnight. Then, samples are transferred to gelatin capsules for solidification at 37, 45 and 60 for 24 h, respectively. The samples are sectioned to ~70 nm and attached to copper grids with Formvar film (300 mesh). At last, the sections are performed staining with 2 % uranyl acetate for 30 min and 3 % lead citrate for 30 min, respectively. HT7700 Transmission electron mciroscope (Hitachi, Japan) was used for observation.

Confocal laser scanning microscopy (CLSM).

Under a humidified atmosphere containing 5% CO_2, Panc-1 cells are cultured in a confocal microscope dish in DMEM containing 10% FBS and 1% penicillin-streptomycin at 37 °C for 24 h. Cells are first treated with Cy-5 or DBD labeled conjugates (10 µM for KLAK) and washed with PBS three times. For US irradiation group, the cells are treated by US irradiation (1.0 MHz, 1.5 W/cm^2, 50% duty cycle, 1 min) and incubated for another 3 h. The cells are then treated with Mitotracker Green (200 nM) for another 30 min. Finally, the cells are washed three times with PBS and imaged by a CLSM (Zeiss LSM710) with an oil 63× objective lens.

Cytotoxicity.

The cytotoxicity assay is performed by CCK-8 assay against Panc-1 cells. Panc-1 cells are seeded in a 96-well culture plate (6000 cells/well) with 100 µL DMEM for 24 h, and the cells are exposed to conjugates with or without US irradiation at a series of concentrations for another 48 h. Then, 10 µL of CCK-8 solutions are added to each well and further incubated for 2 h. The concentration of the proliferating cells in each well is confirmed using a microplate reader at test wavelength of 450 nm and a reference wavelength of 690 nm, respectively. The values are expressed as mean ± SD (N = 3). Asterisks (*) denote the statistical significance, which are obtained by the student t-test. The relative cell viability is calculated according to the following equation:

$$Cell\ viability\ (\%) = (A_{samples} - A_0)/(A_{control} - A_0) \times 100$$

Where $A_{samples}$ is obtained in the presence of samples extract solutions and A_0 is obtained with complete DMEM.

In vivo and ex vivo imaging.

All the animal experiments are performed complying with NIH guidelines for the care and use of laboratory animals and the experimental protocol are approved by the Institutional Animal Care of National Center for Nanoscience and Technology. The female BALB/c nude mice (6-week-old) are random allocated to each group, and Panc-1 cells (1×10^7/well) suspended in 100 µL DMEM are inoculated subcutaneously into the hind leg of each mice. Caliper measurements are utilized for estimating the tumor size of the nude mice, and the transplanted tumor grows until a volume about 100 mm^3, 200 µL of Cy5-labeled conjugates (1 mg mL^{-1}) are injected into the mice through tail vein injection. Near-infrared imaging is carried out at predetermined time points (2 h, 4 h, 6 h, 8 h and 12 h) using in vivo spectrum imaging system (excitation filter, 630 nm; emission filter, 670 nm). Mice treated with PBS are acted as the control group. At 12 h, animals are sacrificed, and major organs (tumor, heart, liver, spleen, lung and kidney) are excised for ex vivo imaging and analysis. The values are expressed as mean ± SD (N = 3). Asterisks (*) denote the statistical significance, which are obtained by the student t-test.

The measurement of the distance between nanovesicles and vessels

The estimation of the penetration distance of the materials were based on previous reports (Liu et al., 2018). The simulated scatter diagrams were drawn based on the fluorescence images using Photoshop CS6. The green points represent the vessel, the red points represent the conjugates for each group, respectively, and the white points represent the colocation of the vessel and the conjugates. Using a Rectangular Plane Coordinate System, the coordinate (X, Y) of every point can be known easily. According to the coordinate, we worked out the minimum distance between every red point and its nearest green point, using the followed formula.

$$D = \sqrt{(X_{red} - X_{Green})^2 + (Y_{red} - Y_{Green})^2}$$

Finally, after counting red points from several fluorescence images of each sample, the average value was given as the penetrating distance of the conjugates in each group.

In vivo anti-tumor efficiency in subcutaneous tumor model

The Panc-1-xenografted mice models are established according above method and using female BALB/c nude mice. When the volume of transplanted tumor grows to 50-70 mm^3, the mice are divided into four groups (N = 6) randomly and intravenously injected by PBS, PPK, PK, PTPK (200 μL, 400 μM for KLAK). All the group are treated by US irradiation (1.0 MHz, 1.5W/cm^2, 50% duty cycle, 5 min) at 3 h and 6 h after injection of conjugates. The conjugates are administered to the mice via the tail vein every other day (days 0, 2, 4, 6, 8, 10, and 12). During the treatment process, the tumor volumes and body weight are measured by caliper every other day. The values are expressed as mean ± SD (N = 6). Asterisks (*) denote the statistical significance, which are calculated by post-hoc tests.

In vivo anti-tumor efficiency in orthotopic tumour model

Orthotopic tumours in Balb/c nude mice are transplanted to mimic the natural pancreatic cancer microenvironment. Briefly, after mice are anaesthetized, Panc-1-luc cells are injected into the pancreas head of Balb/c nude mice using a micro-syringe (Hamilton). Two weeks after the tumor implantation, the mice are randomly divided into four groups: saline; free PBS, PPK, PK, PTPK (N = 6 mice per group), and treated with systemic administration of different conjugates (200 μL, 400 μM for KLAK) via tail vein injection every 2 days for 7 injections. All the group are treated by US irradiation (1.0 MHz, 1.5W/cm^2, 50% duty cycle, 5 min) at 3 h and 6 h after injection of conjugates. The body weights of the mice are monitored over the experiment period. The growth of orthotopic tumours is monitored by BLI (Xenogen IVIS Spectrum). Bioluminescent signal is a result due to the reaction of luciferase from Panc-1-luc cells with the D-luciferin (150 mg kg^{-1}, Promega), which was intraperitoneally injected into mice 8-10 min before the imaging. BLI images of the mice are performed at day 14, 19, 24, 29 and 34 after post-tumor implantation. On day 34, the mice are killed and tumor xenografts are collected for ex vivo analyses.

Supplemental References

Cheng, D. B., Zhang, X. H., Y. Gao, J., Ji, L., Hou, D., Wang, Z., Xu, W., Qiao, Z. Y., and Wang, H. (2019). Endogenous reactive oxygen species-triggered morphology transformation for enhanced cooperative interaction with mitochondria. J. Am. Chem. Soc. *141*, 7235-7239.

Liu, F. H., Cong, Y., Qi, G. B., Ji, L., Qiao, Z. Y., and Wang, H. (2018). Near-infrared laser-driven in situ self-assembly as a general strategy for deep tumor therapy. Nano Lett. *18*, 6577-6584.